A&A 475, 281–300 (2007)
DOI: 10.1051/0004-6361:20077889

Astronomy & Astrophysics

Herbig-Haro flows in B335⋆,⋆⋆,⋆⋆⋆,†

M. Gålfalk and G. Olofsson

Stockholm Observatory, Sweden
e-mail: magnusg@astro.su.se

Received 15 May 2007 / Accepted 7 September 2007

ABSTRACT

Aims. To study the Herbig-Haro flows in the nearby dark globule B335. To find new HH objects and H_2 knots, make a proper motion map of the flow activity and investigate physical properties through shock models.
Methods. We have observed optical (Hα and [SII]) and near-IR (2.12 μm H_2) deep fields and taken optical spectra using the 2.56 m Nordic Optical Telescope, as well as a near-UV deep field (U band) using the 3.58 m NTT. In addition we present new SPITZER / IRAC (3.5–8.0 μm) and MIPS (24 μm) observations. We use previous Hα and 2.12 μm H_2 observations taken 15 and 9 years earlier to make proper motion maps. We then investigate the shock physics by matching our spectra with planar shock models.
Results. We discover five new HH objects (HH 119 D–H) in the eastern and one (HH 119 I) in the western lobe of the outflow. From proper motions we find an optically bright, roughly E–W oriented group with high space velocities (200–280 km s^{-1}) and a near-IR bright, slower group (15–75 km s^{-1}) moving to the ESE. We also find a system of at least 15 H_2 knots in the western lobe. This (WNW) counterflow suggests the possibility of a binary outflow source, giving rise to two outflow axes with slightly different orientations. We find that the E–W flow is symmetrical with evidence for two outbursts. We make the first detection of [OI] $\lambda\lambda$ 6300/63 in HH 119 B and Hβ in HH 119 A and B and find their extinctions to be $A_V \approx 1.4$ and 4.4, respectively. HH 119 A is found to expand much faster than expected from linear expansion with distance from the outflow source. Using planar shock models we find shock velocities of ∼60 km s^{-1} (A) and ∼35 km s^{-1} (B and C). This agrees with A being of higher excitation than B and C. In our U image we detect three of the HH objects and propose that the emission arise from the [OII] λ3728 line and the blue continuum. New SPITZER / IRAC and MIPS observations show most of the HH objects at 4.5 μm and a E–W elongated hour-glass shaped structure at the outflow source. Even at 24 μm it is not clear whether most of the light is direct or reflected.

Key words. ISM: jets and outflows – infrared: ISM – ISM: lines and bands – stars: formation – ISM: individual objects: B335 – ISM: individual objects: HH119

1. Introduction

The nearby prototypical globule B335 is located at about 250 pc, as estimated from star counts (Tomita et al. 1979). It is very isolated and contains a deeply embedded, low-luminosity, low-temperature outflow source (Frerking & Langer 1982). The extinction towards this central outflow source is extremely large ($A_V > 320$ mag, e.g. Chandler et al. 1990). This explains why the central object has only been seen at far-IR (Keene et al. 1983) and longer wavelengths. It has been observed in sub-mm (Chandler et al. 1990) and at 3.6 cm using the VLA with increasing resolutions, Anglada et al. (1992) (config D, ±9″), Avila et al. (2001) (config C, ±3″) and Reipurth et al. (2002b) (config A, sub-arcsec resolution). These observations have shown that the source is variable over timescales of years (Avila et al. 2001). Reipurth et al. (2002b) found the outflow source to be clearly elongated at 3.6 cm in the east-west direction, along the outflow axis, indicating a compact thermal radio jet. The combined observations makes the B335 outflow source one of the clearest examples of a so-called Class 0 source (André 1993), the earliest evolutionary phase of star formation, in which a deeply embedded protostar and a bipolar outflow exists.

The central ∼1 × 1′ has previously been observed in deep H and K band images using both Keck I (Hodapp 1998) and the HST (Harvey et al. 2001). Observational evidence for current protostellar collapse also exists, based on millimetre wave interferometry (Harvey et al. 2003).

B335 is ideal for a case study of isolated star formation, as there is absolutely no source confusion caused by OB stars or outflows from other young stars, unlike most star forming regions. Its geometry is similar to that of the well-known HH 30 (disk and outflow), being seen almost exactly from the side it also contains a bipolar molecular outflow accompanied by several Herbig-Haro (HH) objects lying in a line with roughly constant declination through the deeply embedded outflow source. The axis of this HH flow coincides with that of the molecular outflow. However, as can been seen in an optical deep field of B335 (e.g. the one in this paper) the extinction drops off rapidly about one arcminute from the centre, making it possible to do optical spectroscopy of several of the HH objects.

The three HH objects known prior to this paper are called HH 119 B (discovered as a HH candidate by Vrba et al. 1986; and confirmed by Reipurth et al. 1992) and HH 119 A and C (Reipurth et al. 1992). Hodapp et al. (1998) discovered several

⋆ Based on observations made with the Nordic Optical Telescope, operated on the island of La Palma jointly by Denmark, Finland, Iceland, Norway, and Sweden, in the Spanish Observatorio del Roque de los Muchachos of the Instituto de Astrofisica de Canarias.

⋆⋆ This work is based in part on observations made with the Spitzer Space Telescope, which is operated by the Jet Propulsion Laboratory, California Institute of Technology under a contract with NASA.

⋆⋆⋆ Based on observations made with the New Technology Telescope, ESO (La Silla) under programme ID 077.C-0524.

† NOT and NTT images in FITS format are only available in electronic form at the CDS via anonymous ftp to
cdsarc.u-strasbg.fr (130.79.128.5) or via
http://cdsweb.u-strasbg.fr/cgi-bin/qcat?J/A+A/475/281

H_2 features (called HH 119 IR 1–5) using the 2.12 μm line of H_2. In this paper we contribute with a detailed investigation of the B335 HH flows using mid-IR Spitzer data, deep near-UV, optical and near-IR imaging and optical spectra, revealing six new HH objects (two with previously seen near-IR counterparts). We calculate the proper motion of HH objects and H_2 features and for HH 119 A–C we use planar shock models to calculate shock velocities, shock compression, preshock densities and extinctions.

2. Observations and reductions

2.1. Ground based

All our ground based observations, except the near-UV imaging, were carried out at the 2.56 m Nordic Optical Telescope (NOT) located at 2382 m above sea level on the island of La Palma, Canary Islands. We have used the two cameras ALFOSC (Optical spectroscopy and imaging) and NOTCam (Near-IR imaging). The near-UV deep field was obtained at the 3.58 m New Technology Telescope (NTT) located at La Silla Observatory, Chile. For details, see the subsections below.

2.1.1. Optical spectra

The ALFOSC (Andalucia Faint Object Spectrograph and Camera) long-slit spectra along the optical Herbig-Haro flow of HH 119 in B335 were obtained 16 May 2003 using grism #7 (3850–6850 Å) with a slit width of 2.″5 (R = 260). This slit width was suitable since the centres of HH 119 A–C have the same declinations within 1.″3 of each other, however, HH119 A is extended but with a condensation to the south (HH119 A_2; Reipurth et al. 1992) that was located inside the slit. With a slit length of 6.′5 it was possible to observe all three objects in one slit for a total exposure time of 2400 s. Even though the Moon was full, this did not influence the spectra noticeably since a total lunar eclipse was in fact occurring at the time of the observations. ALFOSC has a 2048 × 2048 array with a pixel size of 0.″188 and the seeing was about 1.″0 during the observations. There were only three known HH objects (A–C) at the time of the observations, but a fourth HH object (D), east of object C, was also within the slit due to the alignment of the slit along constant declination.

2.1.2. Near-IR deep field (2.12 μm H_2)

We have made deep near-IR observations of B335 using the 2.12 μm $\nu = 1-0$ S(1) line of H_2. In order to use as much telescope time as possible for the line observations, the corresponding continuum observations were made using a K_S filter (2.14 μm central wavelength). The observations were made during 4 photometric nights, 4−8 July 2004, under seeing conditions that varied from poor to excellent. We used nb exposure times of 119 s and K_S (continuum) exposures of 32 s to avoid saturation in most bright stars. These exposure times had been tested on a previous run and were shown to keep the near-IR camera, NOTCam, within its linear regime throughout most of the image, without any large transient effects from bright sources that could otherwise have made a strong pattern in the mosaic from the dithering involved. After careful selection of all exposures, based on seeing, the final mosaic is both deep and sharp, with a mean seeing of 0.″68 and total central mosaic exposure times of 23 205 s (6.45 h) and 2880 s (48 min) for the 2.12 μm line and K_S band respectively.

NOTCam is an HAWAII 1024 × 1024 × 18.5 μm pixel HgCdTe array with a field-of-view of 4.′0 × 4.′0 (pixel size of about 0.″23). Since the observations are used for proper motion calculations we applied a distortion model for NOTCam (Gålfalk 2005) using only the very sharpest exposures by mapping a relation between the on-CCD pixel positions of all known 2MASS stars in the field to their known coordinates. Using this model we have successfully removed most of the previously seen distortion, and even at the mosaic edges the PSF of stars is circular.

A median sky is subtracted from the target (with equal exposure time) and in these observations, where we do not have any really extended objects, we use small-step dithering between each exposure and calculate a median sky from the on-frames themselves. This effectively more than doubles the on-target telescope time when compared to beam switching. The flatfielding is also differential (skyflats observed with some time delay and subtracted). Besides the usual reduction steps of near-IR imaging, using in-house routines (written in IDL), we also wrote subroutines to find and remove bad pixels, remove image distortion, sub-pixel shifting and adding overlapping images to a mosaic taking into account pixel weighting of individual pixel exposure times. We also made a routine to remove any dark stripes that results from lowered sensitivity after a bright source has been read out of the CCD – this could go unnoticed for normal imaging but when a deep field is made with a lot of overlaps this can introduce a complicated pattern (especially after distortion correction) that has to be removed in order to be able to keep a high contrast throughout the mosaic.

The two mosaics were then sub-pixel shifted in order to coincide, scaled in brightness relative to each other and a constant added in order to emphasize H_2 line emission by having the same background levels in both filter mosaics and setting a suitable contrast. The final image is a colour composite made by RGB colour coding the line image into the red and green channels and the K_S (continuum) image into the blue channel, resulting in a deep image (Fig. 1) where H_2 emission features are clearly yellow while stars, galaxies and reflection nebulae are made white/blue.

2.1.3. Western near-IR field (2.12 μm H_2)

In May 2007 we made additional S(1) observations, also using NOTCam, centred on HH 119 A which had not been imaged before at near-IR wavelengths. This was also an attempt to find new H_2 knots in the western outflow. The observations were carried out on May 28 with total on-target exposure times of 90 min in S(1) and 19.7 min in K_S. The reductions were made in a similar way as desribed in the S(1) deep field section (cf. Sect. 2.1.2). The seeing was excellent (0.31–0.″45 in K_S) throughout the night. Part of the resulting image can be seen in Fig. 2 which shows three near-IR counterparts of HH 119 A and a new system of at least 15 S(1) knots to the west.

2.1.4. Optical deep field (Hα and [SII])

As a follow up to the near-IR nb-imaging we have also made deep optical nb-observations in Hα and [SII] 6717/31. In addition we have made corresponding R band observations to sample the continuum for both nb filters. The observations were obtained under good seeing conditions (average seeing 0.″83) during 3 photometric nights, 3−6 Aug. 2005 with ALFOSC

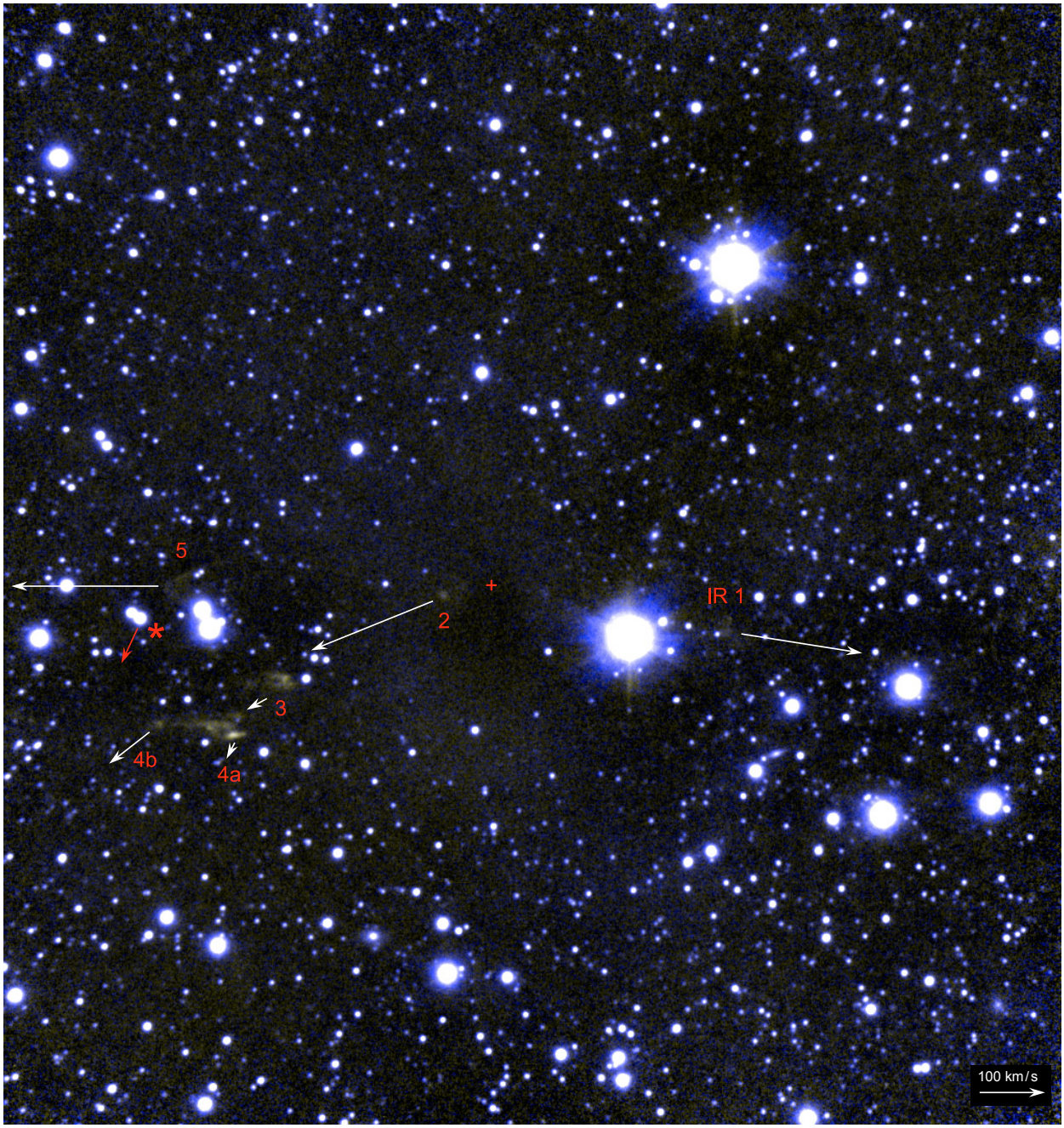

Fig. 1. Near-IR deep field of B335 in the 2.12 μm S(1) line of H_2 (yellow) and K_S (blue) representing the continuum. All previously known H_2 features are confirmed to belong to the bipolar outflow and their proper motions are shown by the arrows. The red arrow shows the high proper motion of a star (asterisk). The position of the outflow source as seen by VLA in the 3.6 cm continuum is marked with a plus sign. The proper motions are divided into two groups, HH 119 IR 1 and 5 moving along constant declination (similar to the optical HH flow) and IR 2–4 moving more to the south east. However, the groups emanate from the same outflow source, as suggested by their proper motions and the cone-like feature at IR 2, with IR 2–4 and IR 5 being on opposite sides of a cone shaped cavity created by the outflow. The field of view is 3.′89 × 4.′13.

(Andalucia Faint Object Spectrograph and Camera). This instrument has a 2048 × 2048 CCD and at a PFOV of 0.″188/pixel it has a FOV of about 6.′4 × 6.′4. For both nb filters we used an exposure time of 600 s and for the *R* band 60 s was used in order to avoid too much saturation of bright stars. The resulting three mosaics have total central exposure times of 24 000 s (6.67 h) Hα, 22 200 s (6.17 h) [SII] and 2340 s (39 min) for the *R* band (continuum).

In addition to the usual reduction steps of optical imaging (bias removal, flatfielding, cosmic ray removal) using our own set of in-house IDL routines, we also made a camera distortion model for ALFOSC using our sharpest exposure and the positions of 163 USNO-A2 calibration stars. After distortion removal, all exposures in each filter were sub-pixel shifted and combined, resulting in three mosaics. The final colour composite mosaic was made with the RGB colour coding Hα (red channel), [SII] (green channel) and *R* band (blue channel). Efforts were made to achieve a high contrast in the final mosaic, with the same background level in all channels outside of nebulous regions and a colour scaling that makes most stars white, nebulae blue, Hα and [SII] emission features clearly red and green, respectively.

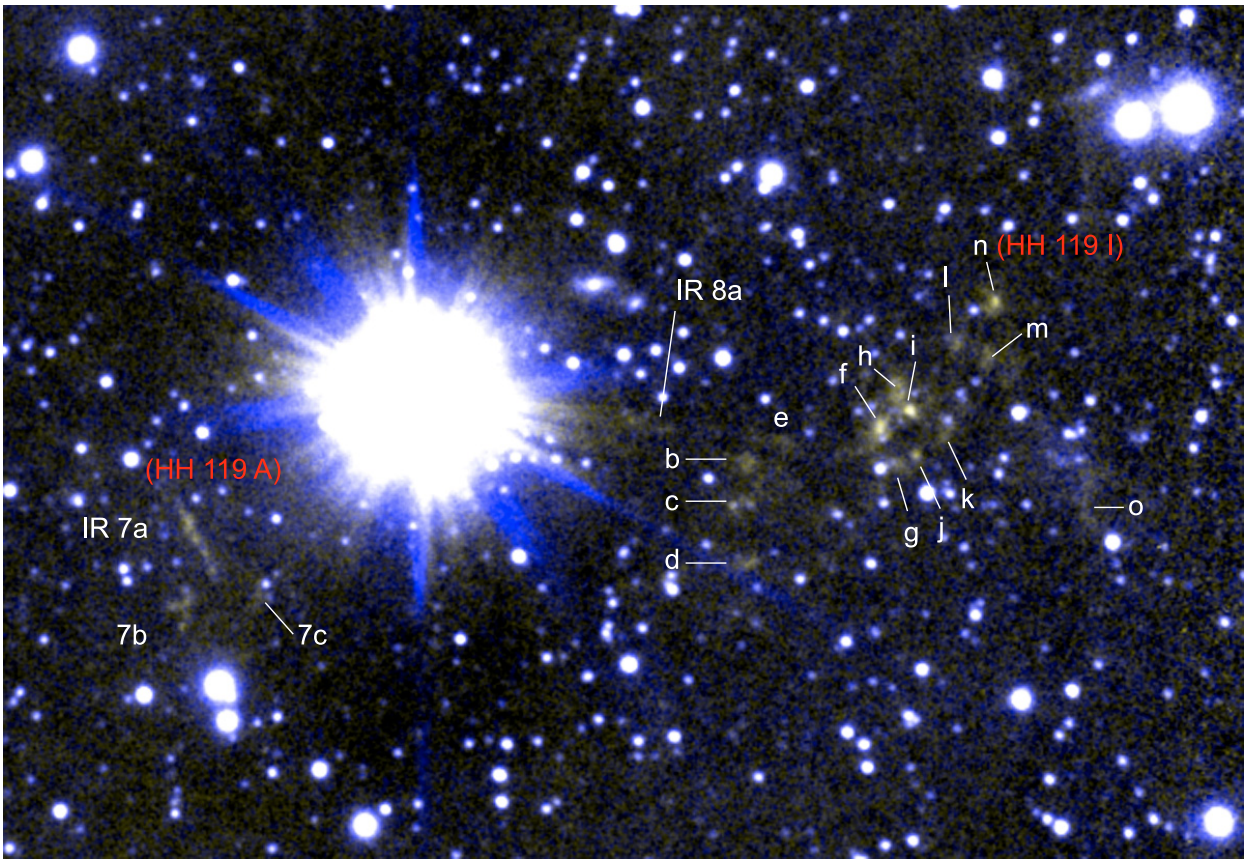

Fig. 2. Near-IR image of western B335 in the 2.12 μm S(1) line of H_2 (yellow) and K_S (blue) representing the continuum. A near-IR counterpart of HH 119 A (which we call IR 7) is found as well as an extended new system of S(1) features further to the west. The HH 119 A counterpart consists of three parts, two fairly bright S(1) features (IR 7a and b) reminiscent of the optical shock but clearly broken up and a fainter part (7c) coinciding with a region of extended [SII] emission in the optical. We find 15 S(1) knots (IR 8a–o) in the extended S(1) feature to the west, one (IR 8n) which is also seen in Hα and [SII] (Fig. 4) and classified as an Herbig-Haro object (HH 119 I). The field of view is 2.′30 × 1.′58.

The resulting colour mosiac is shown in Figs. 3 and 4. All the detected Herbig-Haro objects, except HH 119 I (Fig. 4), are shown in more detail in Fig. 5.

2.1.5. Near-UV deep field

Using EMMI on the 3.58 m New Technology Telescope (ESO) during four nights, 28 Jun.−01 Jul. 2006, we have obtained 37 × 720 s exposures of B335 in the *U* band, resulting in a total exposure time of 26 640 s (7.4 h). The filter, U602, is a Bessel *U* band filter centred on 3542 Å (covering roughly 3100−4000 Å) and its transmission curve is shown in Fig. 6. The usual reduction steps of optical reductions were applied, including bias removal, flat fielding and shift-and-add to correct for tracking errors and small-step dithering between images. The sigma-clipping technique was used to remove all cosmic rays after making the sky mean value equal in all exposures.

The EMMI-Blue/NTT 1024 × 1024 chip gives a pixel and image field of view of 0.″362 and 6.′2 × 6.′2, respectively. The average airmass in these observations is 1.35 and the average seeing 2.″03.

2.2. Spitzer space telescope

Spitzer is an IR space telescope that carries a 85 cm cryogenic telescope and three cryogenically cooled science instruments, one of these is the Infrared Array Camera (IRAC) that provides simultaneous 5.′2 × 5.′2 images in four channels, centred at 3.6, 4.5, 5.8 and 8.0 μm. Each channel is equipped with a 256 × 256 pixel detector array with a pixel size of about 1.″2 × 1.″2. Another instrument is the Multiband Imaging Photometer for Spitzer (MIPS) that contains three separate detector arrays, making simultaneous observations possible at 24, 70, and 160 μm.

The Spitzer data used in this paper (see Table 1) were obtained from the Spitzer Science Archive using the Leopard software. All data had been reduced to the Post-Basic Calibrated Data (pbcd) level. We use all channels of the IRAC observations, and some in-house routines to reduce them further and especially to make a colour composite image. From the MIPS data, we only use the 24 μm observations because of its higher resolution and because the other two channels are full of artefacts (probably due to saturation). The 24 μm camera has a format of 128 × 128 pixels and a pixel size of 2.″55. In order to plot Spitzer contours on our ground-based observations, although very different resolutions, we matched all stars seen in the Spitzer 24 μm mosaic with both our K_S and *R* band observations and corrected for differences in FOV, distortion and image rotation.

2.3. Proper motions

2.3.1. Near-IR first epoch image

In order for us to map the IR proper motions of as many H_2 features as possible we needed a previous epoch of 2.12 μm observations, having a long enough time span to show the proper

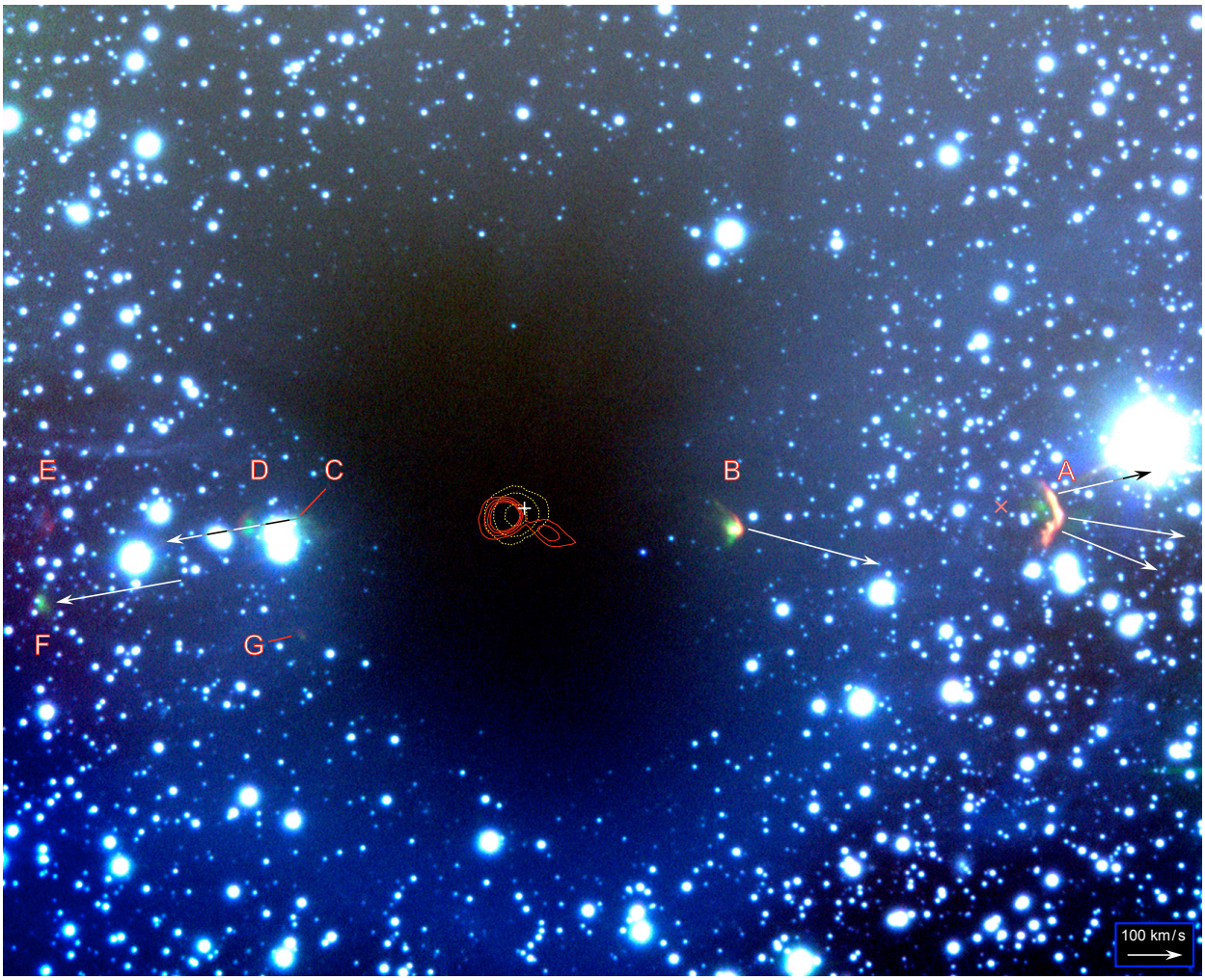

Fig. 3. Optical deep field of B335 using a composite of Hα (red), S[II] (green) and the *R* band (blue). The first thing we note is that the molecular cloud surrounding the globule shines unevenly across the image, with both nebulous patches and hole-like features. This is probably caused by scattered starlight (in the *R* band). HH 119 A–E are located in an almost perfect line along constant declination, with proper motions showing them to be part of the same bipolar HH flow. Note that the proper motion arrow for object F is displaced to fit inside the figure. The Spitzer contours show the outflow source region at 8.0 μm (red, solid curves) and 24 μm (yellow, dotted curves). The VLA outflow source position is marked with a white plus sign. At 8.0 μm there is a clear bipolar-like feature caused by reflected light whereas the 24 μm observations have a single peak with a location close to the VLA source. The red cross marks the origin HH 119 A *would have had* based on its current expansion alone (Fig. 12), suggesting that this bow shock is currently expanding much faster than before. The field of view is 5.′18 × 4.′20.

motions with reasonable accuracy, but at the same time with high enough quality to show as many of our recently observed H_2 objects as possible given that the new epoch is a deep field. We would like to thank Klaus-Werner Hodapp for kindly providing us with the first epoch observations, in the form of a deep (8200 s or about 2.3 h) mosaic taken with the 2.2 m University of Hawaii telescope. These observations were made using the Quick Infrared Camera (QUIRC) mounted at the f/10 focus, yielding a pixel size of 0.″185 (not that far from our second epoch images, 0.″23). Since these observations were obtained between 8−10 July 1995 (and our second epoch observations 4−8 July 2004) we have a time span of about 9 years between the epochs. For more information about the first epoch observations see Hodapp et al. (1998).

2.3.2. Optical first epoch image

For our optical proper motions, we used an even larger time span (roughly 15 years) than for the IR case. We would like to thank Bo Reipurth for kindly providing us with the original Hα images from Reipurth et al. (1992), taken in August 1990 with the 3.58 m New Technology Telescope (NTT). These observations are deep enough and have a long enough time span when combined with our images to yield accurate proper motions. The instrument used in these observations, EMMI, provided a field size of 7.′5 × 7.′5 when used with a Thompson 1024 × 1024 pixel chip, yielding a pixel size of 0.″44 (rougly twice the pixel size of our Aug. 2005 observations).

2.3.3. Calculations and accuracy

We refer to Sect. 3 in Gålfalk & Olofsson (2007) for details on our method for calculating proper motions. In short, we fit all stars seen in both epoch images using a two-dimensional elliptical Gaussian. Stars with measurable proper motions are eliminated in the solution. After warping the lower resolution image to fit the one with higher resolution, the images are shifted for each object in sub-pixel (0.1 pixel) steps until the object overlaps

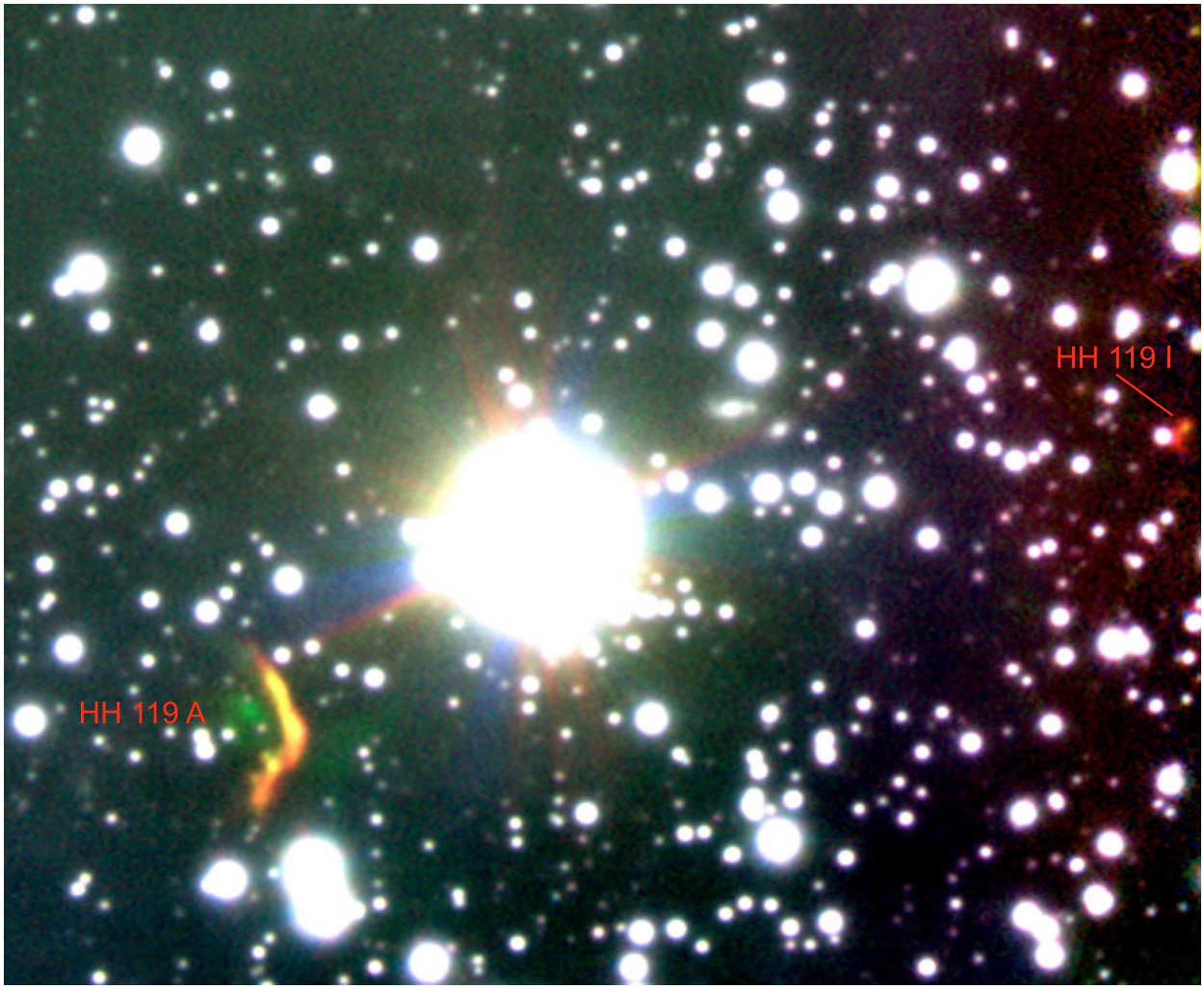

Fig. 4. The westernmost part of our Hα (red), S[II] (green) and *R* band (blue) deep field. The number of exposures and therefore S/N decreases to the west because of flat field uncertainties and image dithering during the observations. After correcting for background variations most of the extended system of S(1) knots is covered, however, only one of these bright S(1) knots is detected in the optical. This object, IR 8n, is seen in both Hα and [SII] and confirmed as a bona-fide HH object (HH 119 I). The field of view is 1.′95 × 1.′60.

itself in both epochs, and a proper motion is found. For each step the matching is judged by blinking the two images at different rates and by making a colour image using two colour channels (red and blue). The accuracy is similar for our optical and near-IR proper motions (about 12 km s^{-1}), except for HH 119 C (close to a bright star) and HH 119 F (faint in the first epoch image).

3. Results and discussion

3.1. New HH objects and H_2 knots

Using our deep optical and near-IR mosaics, in combination with the proper motions obtained from these and the additional information from optical spectra, we confirm that two of the previously known 2.12 μm H_2 features (IR 4 and 5 in Hodapp et al. 1998) have optical counterparts that are bona-fide HH objects (named HH 119 G and D). Four more HH objects are also discovered in our optical deep field (we call these HH 119 E, F, H and I). These six new HH objects can be seen in Figs. 3–5. HH 119 H was first found as an IR H_2 feature in the Spitzer/IRAC mosaic (Fig. 15). However, it is also faintly detected in Hα (Fig. 5) and given its position in the E–W HH flow it is classified as an HH object.

Many of the HH objects have the appearance of bow shocks with clearly separated Hα and [SII] emission. A summary of all shocks is given in Table 2 and the photometry is presented in Table 3. Only three of these objects, HH 119 A–C, were known HH objects prior to this survey. We have followed the same naming scheme, and named Herbig-Haro objects using letters from D to I.

There is a rough symmetry in HH 119 A–F and H, lying approximately in a line through the outflow source, all at two roughly symmetric projected distances, possibly corresponding to two outburst episodes in the central source. The innermost HH object in the western lobe, HH 119 B (58.″2 from the outflow source), has two counterparts in the eastern lobe, HH 119 C (61.″2) and D (73.″3). The outermost western object, HH 119 A (142.″3), has three counterparts in the eastern lobe, HH 119 E (123.″4), F (126.″4) and H (139.″4). HH 119 G is not located on this line roughly along constant declination, instead this object is moving more to the south east, in the same group as IR knots 2, 3, 4a and 4b (Fig. 1). All these IR knots are likely to have optical counterparts, however, due to the high extinction in this part of

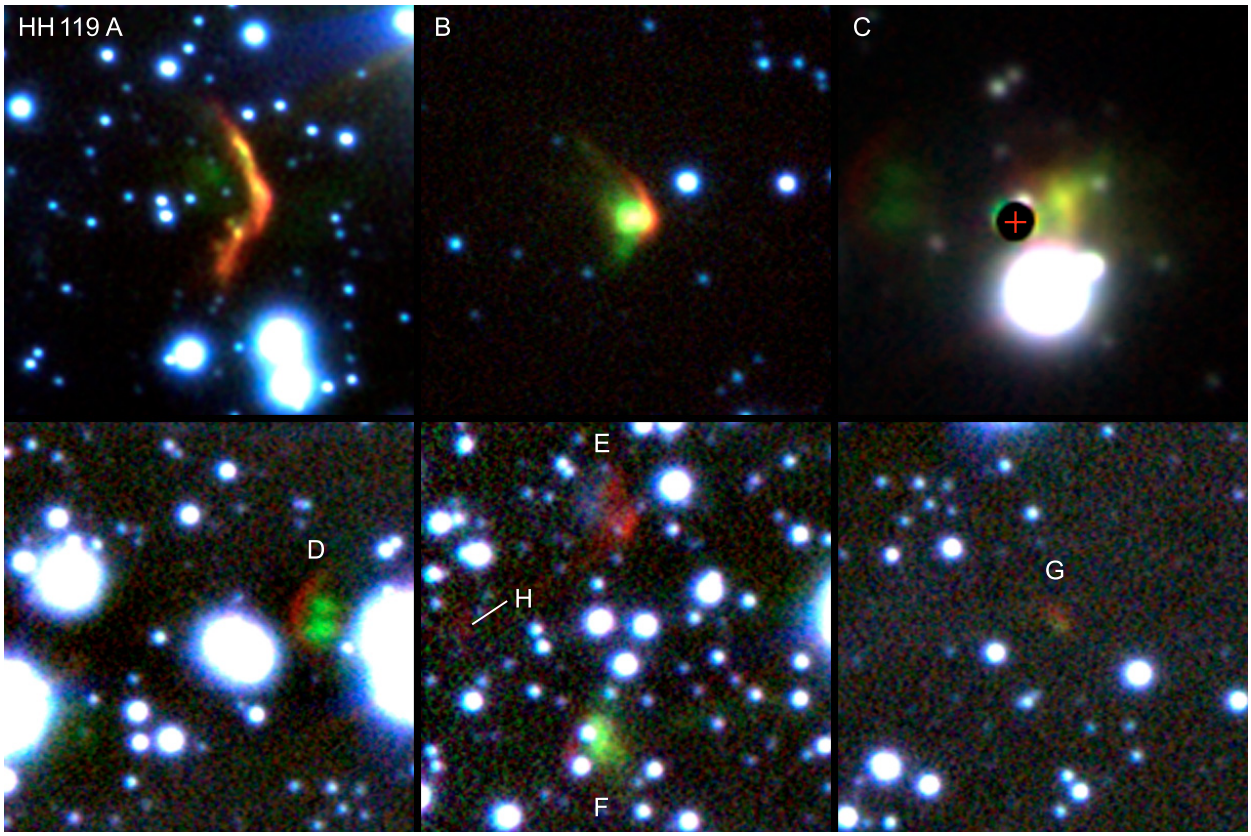

Fig. 5. All Herbig-Haro objects in our optical deep field (HH119 A–H), except object I (See Fig. 4). The colour composition is the same as in Fig. 3. HH119 A and B belong to the west outflow lobe while C–H are part of the eastern lobe. In the case of object C, located very close to a bright star, this star has been removed at the position marked with a red plus sign, using the PSF of another bright star in the image. The central part of the removed star has been blocked out because of strong residuals that could not be removed. Another star can be seen very close to the north of the removed PSF and the C shock itself is fairly extended in both Hα and [SII] and shows no strong condensations. Objects A, B, D and F clearly have Hα bow-shocks leading a [SII] cooling zone, meaning that the flow moves into a less dense ambient medium as opposed to shock G which moves into a denser medium. Object E has a leading shock dominated by a line in the *R* band that is not Hα or [SII], probably [OI] $\lambda\lambda$ 6300/63 emission. The field of view in each panel is 38″ × 38″, except for HH 119 C where the field size is 24″ × 24″.

the flow only knot 4a is detected in the optical and confirmed as an HH object.

In the western lobe we discover a system of 15 new H_2 knots and three counterparts to HH 119 A (Fig. 2).

3.2. Near-IR shocks

Our 2.12 μm H_2 deep field is presented in Fig. 1 along with shock names and arrows illustrating the calculated proper motions. The near-IR proper motions and projected shock velocities are also given in Table 4. There is an apparent division of the shocks into two groups, one (IR 1 and 5) that coincides with the optical HH flow along almost constant declination, and another group (IR 2–4) with a position angle of about 115° (moving to the ESE). The projected velocity vectors suggest that both groups emanate from the outflow source in the centre of B335 (marked by a plus sign in the deep field image). Looking at the east (blue-shifted) lobe, the faint cone-like feature close to the outflow source in the near-IR (Fig. 1) and the mid-IR Spitzer data (Fig. 15), combined with the proper motions suggest that the two groups in the eastern lobe are on the opposite sides of a cone-shaped cavity, cleared out by the molecular outflow.

While the first group (IR 1 and 5) is bright in the optical lines, only the brightest peak in the second group, IR 4a, is seen in our optical Hα and [SII] deep fields. The reason for this could be higher extinction but another reason is hinted by the slower projected velocities, slow moving (C-type) shocks are non-dissociative, instead molecules like H_2 are kept intact and is a good tracer of such shock environments. Fast moving (J-type) shocks instead break up molecules, making such shocks bright in atomic lines such as Hα and $\lambda\lambda$ 6717, 6731 [SII].

West of the outflow source (in the red-shifted lobe) we find at least 16 H_2 knots, one in the deep field (IR 1) and an extended system of knots in the western field (Fig. 2). Although we lack proper motions for this system, they are most likely part of a counterflow to the ESE flow. This suggests the possibility of a binary outflow source, giving rise to both an E–W and an ESE–WNW outflow axis.

The only western knot for which we have previous observations, IR 1, shows a proper motion that points almost exactly away from the VLA outflow source. Although very different in appearance, this shock coincides very well with the southern part of the optically (Hα and [SII]) strong, nicely defined, bow shock HH 119 B. With both the near-IR and optical shocks having a proper motion position angle of roughly 260° and partly overlapping each other, it is clear that they are both part of the same HH flow and originate from the central outflow source. However, how they are physically related is not equally clear from positions and proper motions alone. A similar separation applies for the optical and near-IR images of HH 119 D (IR 5). A more detailed discussion in given in Sect. 3.8 where it is shown that both

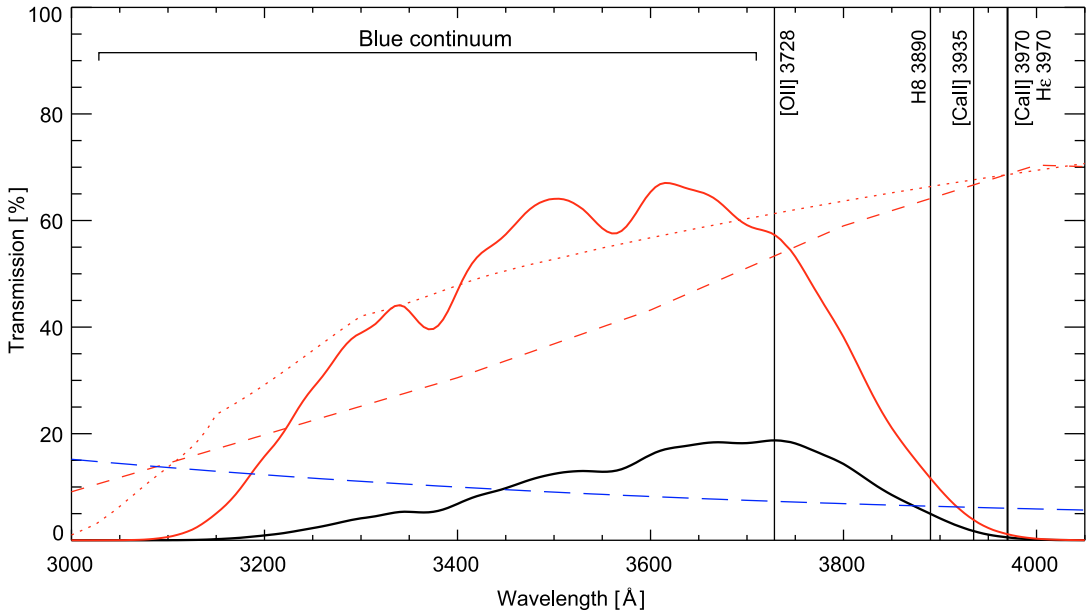

Fig. 6. Transmission curves for the UV observations. The three red curves represent the three major components of the system: atmospheric transmission (dotted), detector QE (dashed) and the Bessel *U* filter (solid). The solid black curve is the total transmission, with all three red curves included. Important emission lines in this wavelength range, seen in UV spectra of HH objects (Hartigan et al. 1999) are marked by vertical lines. The horizontal line roughly marks the most contributing part of the blue continuum and the corresponding spectral energy distribution of the two-photon transition is shown by the blue curve (long dashed) in percentage of its peak value. It is clear that only [OII] 3728 and the blue continuum are likely contributors to the near-UV emission we see from three of the HH objects in B335 (A, B and E).

Table 1. Spitzer archive data used.

Prog.ID	P.I.	Key	Type	Released	Scheduled
94	Lawrence C.	4926464	IRAC Mapping	2005-06-24	2004-04-21
53	Rieke G.	12022016	MIPS Scan Map	2005-11-09	2004-10-15

IR 1 and IR 5 likely trace parts of bow shocks HH 119 B and D, respectively, that have lower shock velocities (i.e. the outer wings of these bow shocks).

3.3. Optical shocks

Our optical deep field (Fig. 3) shows five HH objects (HH 119 A–E) in an almost exact line along constant declination. This is a very clear case of a bipolar HH flow, with proper motions (Table 5) and bow shock morphologies that would be expected from their positions relative to the outflow source. The projected space velocities of the optically bright and neatly lined up HH objects HH 119 A–D (200−280 km s^{-1}) are much faster than the near-IR bright SSE moving groups 3 and 4 (15−75 km s^{-1}).

One explanation for this could be if the fast moving, east-west flow, contains gas expelled into an already cleared out bipolar cone by the outflow source. The optically bright shocks, HH objects, could then be caused by faster gas moving into slower gas (with shock velocities much lower than the space velocities measured from proper motions). However, at the edge of the cone-shaped cavity the expelled gas could interact more with the surrounding globule itself via turbulence, making these near-IR shocks have slower space velocities, almost stationary, due to the encounter with the probably slow moving gas of the globule.

Given that several HH objects are now known on each side of the outflow source, all having similar space velocities, the shocks within each lobe have different dynamical ages and there has thus been *repeated* eruptive episodes where matter from the accretion is expelled into the outflow lobes. Objects B and C are located symmetrically about the outflow source, moving in opposite directions, and were probably expelled in the same outburst. Using their (optical) proper motions and distances from the central VLA source we find dynamical ages of about 250 and 265 years for HH 119 B and C, respectively. The proper motions and dynamical ages of objects B anc C was also measured by Reipurth et al. (1992) who suggested that this outburst may have occurred 350 years ago.

There are four more HH objects seen in the optical deep field, HH 119 F–I. Objects F and H are located in the eastern lobe of the E–W flow, close to the HH 119 A–E line, while objects G (east) and I (west) seem to belong to the tilted (roughly ESE–WNW) flow. HH 119 I is the westernmost object in this flow, and an optical counterpart of an H_2 knot (IR 8n) in a system of at least 15 knots. Since these HH objects (and object D) are new detections, their proper motions are unknown, except for object F which is faintly seen in the Hα first epoch mosaic. Its appearance, bow shaped with a clear separation of Hα and [SII], and its location relative to the outflow source agrees well with the calculated proper motion. The other objects are clearly HH objects even though they lack proper motions, based on their extended nature, separation of Hα and [SII], shapes and locations on the outflow axis. As a further confirmation of HH status for these objects, HH 119 E, G and H are clearly seen in the shock sensitive Spitzer filter centred at 4.5 μm (Fig. 15) along with most of the other HH objects. The reason for this is discussed in Sect. 3.7.

Table 2. Geometry of all Herbig-Haro objects and H_2 knots.

HH 119 [a]	RA [b] (2000)	Dec [b] (2000)	Size [c] ($''$)	Regime	Structure [d]	Reference (first)	Comment
A (IR 7)	19:36:51.32	07:34:10.5	6.1 × 17.2	Optical	Hα / [SII]	Reipurth 1992	Bow shock
(A_1)	19:36:51.32	07:34:10.5	....	"	....	"	Hα peak and background star
(A_2)	19:36:51.47	07:34:06.8	....	"	....	"	Hα peak (South)
(A_3)	19:36:51.46	07:34:15.2	....	"	....	"	Hα peak (North)
B (IR 1)	19:36:56.98	07:34:06.0	8.0 × 13.2	Optical	Hα / [SII]	Vrba 1986	Bow shock
C	19:37:05.00	07:34:06.0	1.7 × 4.4	Optical	Hα + [SII]	Reipurth 1992	No separation between [SII] and Hα
D (IR 5)	19:37:05.82	07:34:07.2	3.7 × 7.2	Optical	Hα / [SII]	This paper	Hα bow shock, two [SII] bullets
E	19:37:09.19	07:34:06.5	5.6 × 8.6	Optical	[SII] [e] / Hα	This paper	Leading feature bright in R band[e]
F	19:37:09.39	07:33:46.0	4.6 × 5.1	Optical	Hα / [SII]	This paper	Bow shock
G (IR 4a)	19:37:04.75	07:33:38.3	2.7 × 2.9	Optical	[SII] / Hα	This paper	
H	19:37:10.22	07:33:56.8	5.4 × 4.4	Optical	Hα	This paper	More extended at 4.5 μm
I (IR 8n)	19:36:45.41	07:34:40.2	2.3 × 3.4	Optical	Hα + [SII]	This paper	Part of a WNW flow
IR 1	19:36:57.22	07:34:01.7	3.0 × 5.4	Near-IR		Hodapp 1998	IR counterpart of HH 119 B
IR 2	19:37:01.50	07:34:08.5	2.3 × 2.4	Near-IR		Hodapp 1998	
IR 3	19:37:03.89	07:33:49.6	11.7 × 3.5	Near-IR		Hodapp 1998	
IR 4	19:37:05.22	07:33:39.3	21.6 × 6.3	Near-IR		Hodapp 1998	Large and irregular
IR 4a	19:37:04.66	07:33:36.6	4.5 × 1.2	Near-IR		This paper	IR counterpart of HH 119 G
IR 4b	19:37:05.77	07:33:39.3	3.7 × 2.1	Near-IR		This paper	Condensation within IR 4
IR 5	19:37:05.70	07:34:09.5	13.8 × 11.5	Near-IR		Hodapp 1998	IR counterpart of HH 119 D
IR 7a	19:36:51.39	07:34:12.7	3.7 × 8.4	Near-IR		This paper	North IR segment of A
IR 7b	19:36:51.53	07:34:05.4	2.8 × 4.7	Near-IR		This paper	South IR segment of A
IR 7c	19:36:50.93	07:34:06.5	2.6 × 3.8	Near-IR		This paper	Segment in front of bow A
IR 8a–o	19:36:46	07:34:26	58 × 33	Near-IR		This paper	Extended system of 15 H_2 knots
IR 8f	19:36:46.23	07:34:27.2	0.9 × 1.6	Near-IR		This paper	One of the brightest knots in IR 8
IR 8i	19:36:46.02	07:34:29.1	0.9 × 0.7	Near-IR		This paper	One of the brightest knots in IR 8
IR 8n	19:36:45.39	07:34:41.4	2.3 × 2.6	Near-IR		This paper	IR counterpart of HH 119 I

[a] Letters designate Herbig-Haro objects, while IR numbers designate H_2 knots.
[b] Optical positions in Hα (04 Aug. 2005) and near-IR positions in 2.12 μm H_2 (06 Jul. 2004; 29 May 2007 for IR 7 and 8).
[c] Approximate bounding box sizes, determined visually.
[d] Leading / trailing flux peak.
[e] The leading feature is easier seen in R than [SII], most likely due to a strong line other than Hα and [SII].

Table 3. Flux summary.

HH 119 (1)	F_U [a] (2)	F [Hα] [b] (3)	F [SII] [c] (4)	F [S(1)] [d] (5)	$F_{4.5}$ [e] (6)	F [SII] / F [Hα] [f] (7)
A (IR 7)	8.50 ± 0.34	17.34 ± 0.91	9.94 ± 0.47	17.12 ± 0.38	93 ± 19	0.573 ± 0.018
B (IR 1)	1.45 ± 0.07	05.92 ± 0.34	7.87 ± 0.44	2.73 ± 0.11	103 ± 13	1.330 ± 0.030
C	...	03.54 ± 0.18	7.36 ± 0.41	...		2.079 ± 0.018
D (IR 5)	...	01.40 ± 0.08	2.45 ± 0.10	10.95 ± 0.17	107 ± 19	1.749 ± 0.077
E	1.23 ± 0.06	00.79 ± 0.06	0.51 ± 0.03	out	40 ± 7	0.65 ± 0.11
F	...	00.78 ± 0.05	2.16 ± 0.12	out	67 ± 8	2.78 ± 0.10
G (IR 4a)	...	0.144 ± 0.007	0.065 ± 0.004	6.91 ± 0.14	45 ± 11	0.45 ± 0.15
H (IR 6)	...	00.07 ± 0.01	...	out	147 ± 17	...
I (IR 8n)	out	01.64 ± 0.06	0.24 ± 0.03	5.58 ± 0.18	out	0.148 ± 0.021
IR 2	...	...	...	1.36 ± 0.03		...
IR 3	...	...	...	7.71 ± 0.15	41 ± 6	...
IR 4	...	...	...	21.59 ± 0.30	134 ± 13	...
IR 4b	...	...	...	2.40 ± 0.05	14 ± 3	...
IR 7a	...	...	...	11.04 ± 0.34	...	...
IR 7b	...	...	...	5.43 ± 0.17	...	...
IR 7c	...	...	...	0.66 ± 0.03	...	...
IR 8f	out	...	...	5.29 ± 0.17	out	...
IR 8i	out	...	...	4.34 ± 0.14	out	...

[a] Integrated U band flux in units of 10^{-15} erg s^{-1} cm^{-2}, effective filter width is 408.8 Å (from total transmission curve).
[b] Emergent flux in Hα, in units of 10^{-15} erg s^{-1} cm^{-2}.
[c] Emergent flux in the 6717+6731 [SII] lines, in units of 10^{-15} erg s^{-1} cm^{-2}.
[d] Emergent flux in the H_2 $\mu = 1{-}0$ S(1) 2.12 μm line, in units of 10^{-15} erg s^{-1} cm^{-2}.
[e] Integrated flux of Spitzer IRAC 2 (4.5 μm) in units of 10^{-15} erg s^{-1} cm^{-2}. HH 119 C and IR2 close to bright sources.
[f] Mean flux ratio including full object extension.

Table 4. IR proper motion results. Column 1 gives the H_2 feature designation, as given in Fig. 1. Columns 2–4 give the angular distance each shock has moved between the two epochs (9 years apart). Columns 5−7 are the proper motions and finally Cols. 8, 9 the (tangential) velocities and positional angles. Uncertainties are given at the bottom of the table (except for the PA which is given for each row).

HH 119	Δ_α	Δ_δ	$\Delta_{\rm tot}$	μ_α	μ_δ	$\mu_{\rm tot}$	vel	PA [a]	Comment
	($''$)	($''$)	($''$)	(mas/yr)	(mas/yr)	(mas/yr)	(km s^{-1})	(deg)	
(1)	(2)	(3)	(4)	(5)	(6)	(7)	(8)	(9)	(10)
IR 1 (B)	–1.51	–0.24	1.53	–168	–27	170	201	261 ± 3	
IR 2	+1.53	–0.61	1.65	+170	–68	183	217	112 ± 3	
IR 3	+0.17	–0.09	0.19	+19	–10	21	25	119 ± 24	
IR 4a (G)	+0.06	–0.11	0.12	+6	–12	14	16	153 ± 37	
IR 4b	+0.45	–0.35	0.57	+50	–39	63	75	128 ± 9	
IR 5 (D)	+1.86	0	1.86	+207	0	207	245	90 ± 2	
Star	+0.17	–0.35	0.39	+19	–39	44	...	155 ± 8	Marked in Fig. 1
	± 0.06	± 0.06	± 0.09	± 7	± 7	± 10	± 12		

[a] Position Angle: North 0°, East 90°, South = 180°, West 270°.

Table 5. Optical proper motion results. Column 1 are the HH designations, as given in Fig. 3. Columns 2−4 give the angular distance each shock has moved between the two epochs (15 years apart). Columns 5−7 are the proper motions and finally Cols. 8, 9 the (tangential) velocities and positional angles. Uncertainties are given at the bottom of the table (except for the PA where this is given in each row).

HH 119	Δ_α	Δ_δ	$\Delta_{\rm tot}$	μ_α	μ_δ	$\mu_{\rm tot}$	vel	PA [a]
	($''$)	($''$)	($''$)	(mas/yr)	(mas/yr)	(mas/yr)	(km s^{-1})	(deg)
(1)	(2)	(3)	(4)	(5)	(6)	(7)	(8)	(9)
A_1	–3.00 ± 0.10	–0.49 ± 0.10	3.04 ± 0.12	–201 ± 7	–33 ± 7	203 ± 9	241 ± 10	261 ± 3
A_2	–2.43 ± 0.10	–0.97 ± 0.10	2.62 ± 0.13	–162 ± 7	–65 ± 7	175 ± 10	207 ± 11	248 ± 3
A_3	–2.34 ± 0.10	+0.53 ± 0.10	2.40 ± 0.12	–156 ± 7	+36 ± 7	160 ± 9	190 ± 10	283 ± 3
B	–3.40 ± 0.10	–0.91 ± 0.10	3.52 ± 0.13	–227 ± 7	–61 ± 7	235 ± 9	278 ± 11	255 ± 3
C	+3.42 ± 0.19	–0.57 ± 0.19	3.47 ± 0.22	+228 ± 13	–38 ± 13	231 ± 15	274 ± 18	100 ± 4
F	+3.23 ± 0.57	–0.57 ± 0.57	3.28 ± 0.66	+216 ± 38	–38 ± 38	219 ± 44	260 ± 53	100 ± 10

[a] Position Angle: North 0°, East 90°, South = 180°, West 270°.

HH 119 E has a different flux distribution than the other HH objects. In Fig. 3 its leading shock is seen more clearly in the *R* band than in [SII] emission (making the leading shock look blue in the mosaic even though the *R* and [SII] position of the shock overlaps, followed by the Hα shock). This is very likely due to unusually bright [OI] $\lambda\lambda$ 6300/63 emission. The situation is similar to HH 119 B, which has bright [OI] emission lines as seen in recent spectra (Fig. 7), but with an even higher [OI]/[SII] ratio since HH 119 B looks red-yellow-green across the shock, using the same colour scaling.

HH 119 G, seen in both Hα and [SII], coincides very well with the brightest peak of the corresponding feature in the near-IR mosaic (H_2 knot IR 4a) and has a separation between Hα and [SII] supporting the near-IR proper motion.

Objects A and E (F) are located roughly symmetrically on opposite sides of the outflow source and may belong to the same outburst, prior to the B and C outburst. We estimate the ages of HH 119 A and F to be about 700 and 590 years, respectively. The difference of about 100 years in these estimates may be due to the large uncertainty in proper motion for object F (which is only faintly detected in the first epoch image).

3.4. Optical spectra and line-ratios of HH 119 A–D

The optical spectra of HH 119 A–D are shown in Figs. 7 and 8. Even though all spectra cover the spectral range 3850−6850 Å, each spectrum has been plotted using individual ranges, omitting parts where no features are seen.

In Table 6 we present calibrated and relative (to Hα) line fluxes for all detected lines. The dereddened flux (F_0) has been calculated using the extinctions we find for HH 119 A and B using planar shock models and comparing the intrinsic and observed Hα/Hβ ratios (cf. Sect. 3.5). We have also calculated the mean electron density, $n_{\rm e}$, in HH 119 A, B and C for the position covered by the slit using the [SII] $I(\lambda6717)/I(\lambda6731)$ line ratio. For this we use the effective collision strengths for electron impact excitation given in Ramsbottom et al. (1996) and Einstein A-coefficients from Keenan et al. (1993), assuming an electron preshock temperature of $\sim 10^4$ K which is a common assumption for HH shock models (see e.g. Morse et al. 1994). The uncertainty range in these estimates are given in paranthesis in Table 6.

All objects show Hα in strong emission and except for HH 119 A, the [SII] 6717/31 doublet is the strongest line. The choice of nb filters for our optical deep fields were in fact based on the line strengths in these spectra. HH 119 A, B and C also have [OI] $\lambda\lambda$ 6300/63 emission lines ([OI] 6300 faintly seen in object D as well but with poor S/N).

It is also very interesting to note that the [OI] lines are strong in HH 119 B. This is somewhat unexpected, as they were not detected in previous spectra by Reipurth et al. (1992) taken 13 years earlier even though the S/N of those observations should have been more than enough for a clear detection. This suggests that the [OI] lines are very variable and that conditions have changed a lot in HH 119 B during this time period. The spectra confirm that object A is an intermediate excitation object while HH 119 B, C and D are found to have lower excitation. Since HH 119 A is located further out from the outflow source than object B, the lower excitation of B could be explained by it moving in the wake of the bow shock from object A.

It is common practice to plot contours of e.g. Hα–[SII] to illustrate regions dominated by Hα (positive) and [SII] (negative), respectively. This has the disadvantage of cancelling out in

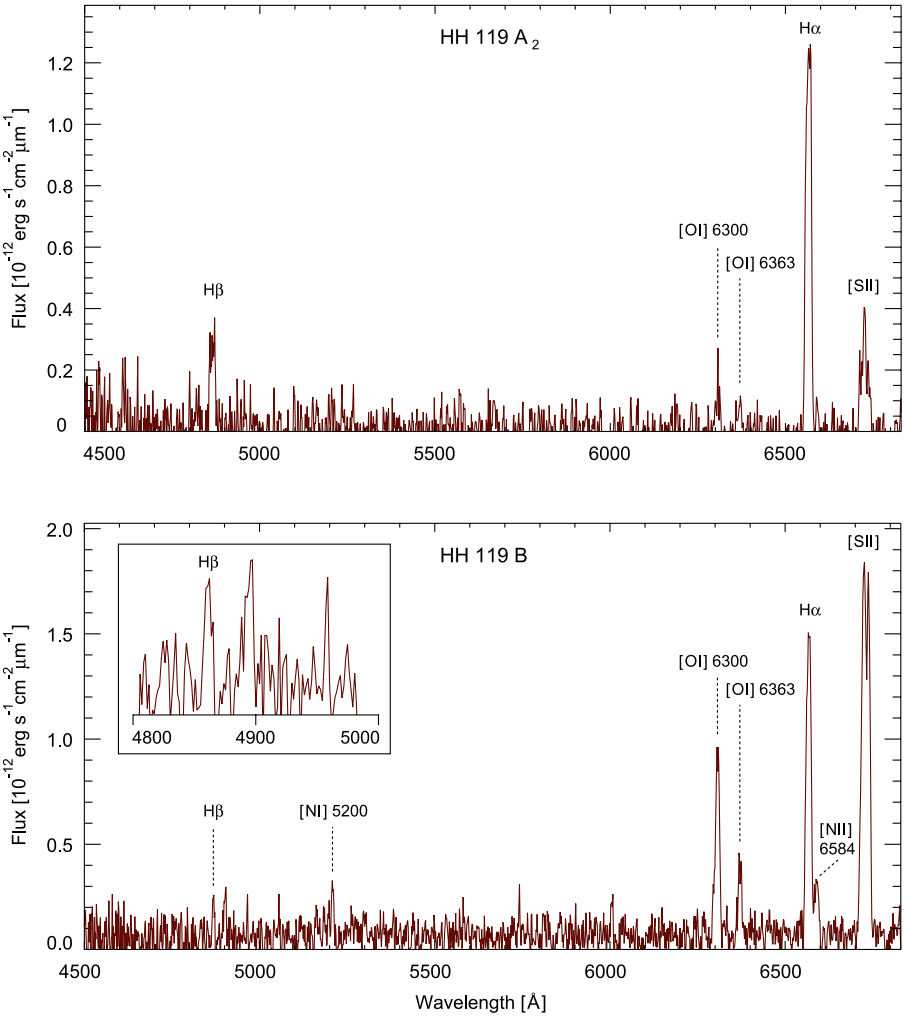

Fig. 7. Optical spectra of HH 119 A and B (NOT/ALFOSC). Object A is clearly of higher excitation than object B. Hβ is detected for the first time in object A and B, as well as strong [OI] lines in HH 119 B that were not seen in spectra taken 13 years earlier (suggesting variable [OI] lines).

regions where Hα and [SII] have similar flux. It also lowers the signal of both the Hα and [SII] contours while the noise remains at the same level. This is the case since they always cancel out partially as long as there is some Hα or [SII] flux present. A map of F([SII])/F(Hα) is better in that respect but has its own disadvantages, the most noticeable one being that very large values (both positive and negative) are found where F(Hα) is close to zero (mostly in sky regions). It is also common to plot Hα+[SII] contours. This uses the full S/N for contours but hides the relative flux information that indicates the abundance of the two species.

A solution to this illustrative dilemma is found by e.g. using coloured contours to simultaneously plot both the total flux F(Hα)+F([SII]) (contours) and their relative strength F(Hα)/F([SII]) (colours). This is presented for HH 119 A and B in Figs. 9 and 10, respectively. Note that the contours are coloured on a pixel-scale level (0.″188) meaning that each contour can have any colours along its curve. By choosing reasonable surface brightness limits for the faintest contour included in the plots only relevant regions are included (i.e. most of the HH object and all stars, while excluding the sky). Technically this is done by multiplying a high-resolution binary contour map (zero for sky and one for contours) pixel-by-pixel with an equally high-resolution F(Hα)/F([SII]) ratio map that has been coloured with red and blue shades to separate Hα (blue) and [SII] (red) bright regions.

From these figures it is clear that HH 119 A is of relatively high excitation compared to HH 119 B which is a low excitation object. There is also a clear separation in both HH 119 A and B, between Hα (leading) and [SII] (trailing) in the direction of motion. In both cases the bow shock is of high excitation (low [SII]/Hα ratio) and the emission behind the bow shock is of low excitation (high [SII]/Hα ratio). This structure is typical for most HH objects, Hα tracing sharp leading edges of the cooling zone and [SII] dominating in the chaotic and clumpy postshock region. It is indicative of a heavy flow that rams into a less dense ambient medium. The situation is the same for all other HH objects in B335, except for E and G which have [SII] leading Hα, suggesting a flow that rams into a denser ambient medium. See Sect. 3.8 for more discussion of the individual HH objects.

3.5. Shock modeling and extinction

In this section we use the planar shock models of Hartigan et al. (1994) with our electron densities and different line ratios (from Table 6) for HH 119 A–C to calculate the average shock velocity ($\langle V_S \rangle$), [SII]-weighted ionization fraction ($\langle I \rangle$), preshock density (n_0), compression (C) and intrinsic (Hα/Hβ)$_0$ ratio of each shock. Using the observed (Hα/Hβ) ratio we also estimate the extinction to HH 119 A and B by applying the optical extinction law described in Cardelli et al. (1989) for $R_V = 3.1$, and calculating the extinction A_V needed to match the intrinsic ratio from the model.

This is an iterative process since we need to know some of the model results, the preshock density n_0 (for the shock

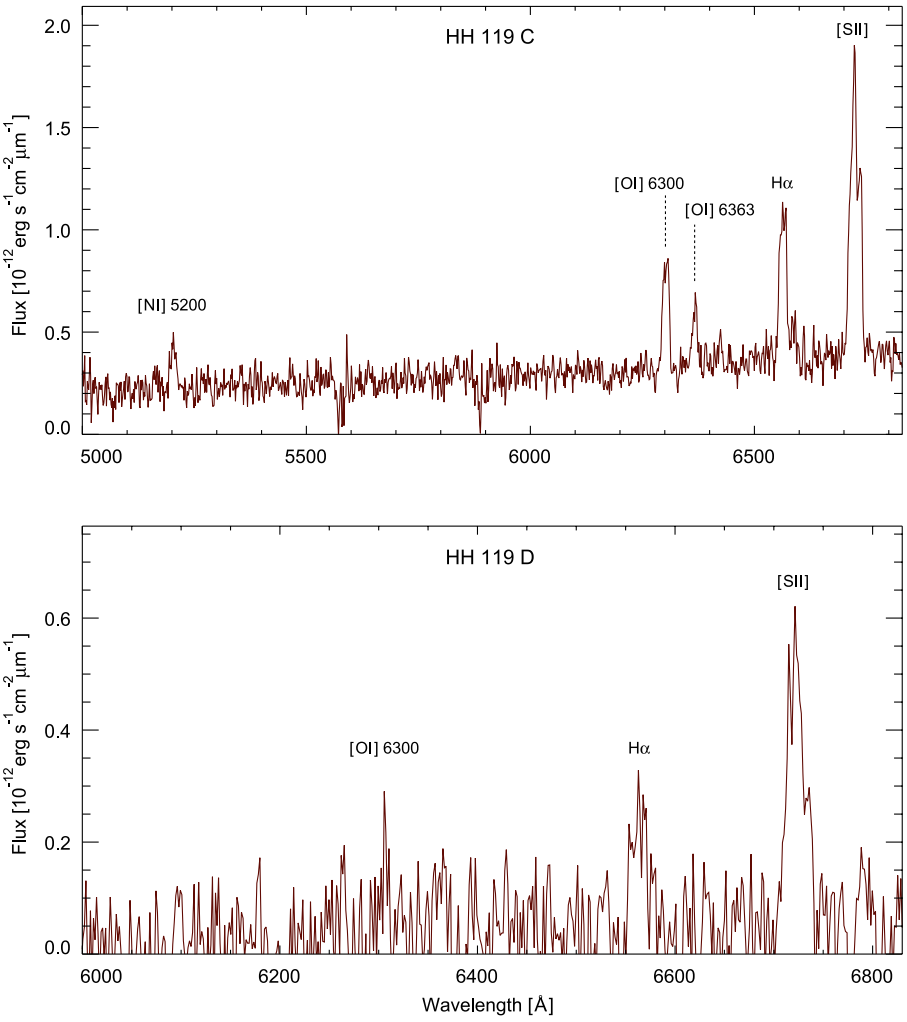

Fig. 8. Optical spectra of HH 119 C and D (NOT/ALFOSC). These are the first spectra of HH 119 C and D, showing both to be of low excitation. HH 119 C is close to a bright star, therefore some continuum is seen in its spectrum.

models) and the $(H\alpha/H\beta)_0$ ratio (to deredden the line ratios) to apply the models to our observations. The preshock density can be found from the models if we can estimate the compression, ionization $\langle I \rangle$ and shock velocity V_S to apply to our electron density since $n_0 = (n_e/\langle I \rangle)/C$. The intrinsic $(H\alpha/H\beta)$ ratio can be assumed to be ∼3 as a first approximation (case B recombination, but usually higher than this for HH objects). By making a few iterations through the shock models and recalculating the extinction and line ratios each time we can get a converging solution. However, for each object we need initial rough estimates of the shock parameters. For this we compare our spectra with the examples given in Hartigan et al. (1994).

HH 119 A is an intermediate excitation object, reminiscent of the HH 47 jet. We therefore start by assuming that $V_S \sim 30\ \mathrm{km\,s^{-1}}$, $\langle I \rangle \sim 2\%$ and $C \sim 20$ (from V_S and the shock models). Using our observationally determined $n_e \sim 250\ \mathrm{cm^{-3}}$ we estimate that $n_0 \sim 625\ \mathrm{cm^{-3}}$. For a (case B) $(H\alpha/H\beta)_0 \sim 3$ and the observed value 5.076 the extinction becomes $A_V = 1.65$ and $E(B-V) = 0.53$. The dereddened line ratios [OI] 6300/Hα, [SII] 6717+31/Hα and [NII] 6583/[OI] 6300 then gives three estimates of V_S, $\langle I \rangle$, C and $(H\alpha/H\beta)_0$, one for each line ratio. These values are then used for the next iteration.

HH 119 B and C are of low excitation, similar to the HH 34 jet (Hartigan et al. 1994), we therefore make the initial estimates $V_S \sim 30\,\mathrm{km\,s^{-1}}$, $\langle I \rangle \sim 1\%$ and $C \sim 15$.

The fact that we do not detect [OIII] λ5007 in any of the objects suggests (Morse et al. 1993) that the shock velocities involved are *lower* than $90\ \mathrm{km\,s^{-1}}$ (for no preionization), $80\ \mathrm{km\,s^{-1}}$ (equilibrium preionization) or $40\ \mathrm{km\,s^{-1}}$ (fully preionized). This, in addition to the excitation types, supports our initial estimates of slow shock speeds ($V_S \sim 30\ \mathrm{km\,s^{-1}}$).

The initial estimates, iterations and results are given in Table 7. Since we do not detect Hβ in the spectrum of HH 119 C its extinction is assumed to be roughly the same as for object B, motivated by the fact that their projected distances from the outflow source are about the same. The resulting extinctions are found to be $A_V = 1.36$ (1.05–1.67), $E(B-V) = 0.44$ (0.34–0.54) for HH 119 A and $A_V = 4.44$ (3.67–5.28), $E(B-V) = 1.43$ (1.18–1.70) for HH 119 B. The assumption that object C has the same extinction as object B based on equal distance from the outflow source may however be inaccurate, as B335 has been shown to have a long tail (Frerking et al. 1987), a remanence from its formation history as a cometary globule (Reipurth 1983). However, since we only use line ratios close to each other in wavelength (a few hundred Å), except for the [NI] 5200/[NII] 6583 ratio, the model results for HH 119 C should not be very sensitive to this assumption.

It is interesting to note that shock velocity and ionization found for object A is much higher than that for object B. This agrees with the suggestion that object B is following in the wake of the outermost object A and thus colliding with cloud material (or turbulence in the flow itself) that has already been sped up by object A. The higher excitation of HH 119 A also agrees with a higher shock velocity and ionization. HH 119 B is found to have

Table 6. Optical spectroscopy.

Object	Line identification	Flux inside slit[a] (10^{-17} erg s^{-1} cm^{-2})	F^b (Hα)	$F_0{}^c$ (Hα)	$F(\lambda6717)/F(\lambda6731)$	$n_e{}^d$ (cm^{-3})
HH 119 A	Hβ λ4861	47.79 ± 4.0	0.197 ± 0.020	0.304 ± 0.035		
	[OI] λ6300	20.04 ± 3.7	0.083 ± 0.017	0.087 ± 0.019		
	[OI] λ6363	11.73 ± 3.7	0.048 ± 0.016	0.050 ± 0.017		
	Hα λ6563	242.1 ± 3.6	1.000	1.000		
	[NII] λ6583	10.45 ± 2.6	0.043 ± 0.012	0.043 ± 0.012		
	[SII] $\lambda\lambda$6717, 6731	75.93 ± 3.7	0.314 ± 0.021	0.304 ± 0.021	1.19 (1.04-1.36)	250 (60-500)
HH 119 B	Hβ λ4861	13.3 ± 3.3	0.056 ± 0.016	0.231 ± 0.087		
	[NI] $\lambda\lambda$5198, 5201	14.19 ± 2.8	0.060 ± 0.013	0.167 ± 0.044		
	[OI] λ6300	121.9 ± 4.4	0.517 ± 0.027	0.611 ± 0.033		
	[OI] λ6363	38.35 ± 4.3	0.163 ± 0.021	0.185 ± 0.025		
	Hα λ6563	235.8 ± 3.6	1.000	1.000		
	[NII] λ6583	26.27 ± 4.2	0.111 ± 0.020	0.110 ± 0.020		
	[SII] $\lambda\lambda$6717, 6731	440.4 ± 4.2	1.867 ± 0.046	1.686 ± 0.043	0.82 (0.76-0.90)	1260 (890-1590)
HH 119 C	[NI] $\lambda\lambda$5198, 5201	27.64 ± 4.4	0.138 ± 0.028	~0.384		
	[OI] λ6300	81.46 ± 4.3	0.408 ± 0.037	~0.482		
	[OI] λ6363	35.07 ± 3.7	0.176 ± 0.026	~0.200		
	Hα λ6563	199.6 ± 7.0	1.000	1.000		
	[NII] λ6583	19.47 ± 5.9	0.098 ± 0.034	~0.097		
	[SII] $\lambda\lambda$6717, 6731	327.3 ± 5.0	1.639 ± 0.085	~1.481	1.29 (1.12-1.40)	140 (30-360)
HH 119 D	[OI] λ6300	16.19 ± 6.8	0.53 +0.44-0.28	...		
	Hα λ6563	30.58 ± 6.7	1.000	...		
	[SII] $\lambda\lambda$6717, 6731	104.2 ± 6.8	3.41 +1.24-0.80	...	...	...

[a] Using a slit width of 2″.5 along constant declination and centred on HH 119 B.
[b] Observed flux, relative to Hα.
[c] Dereddened flux, using the extinction from the model results found in Table 7.
[d] Electron density. Estimate of uncertainty range given in parenthesis.

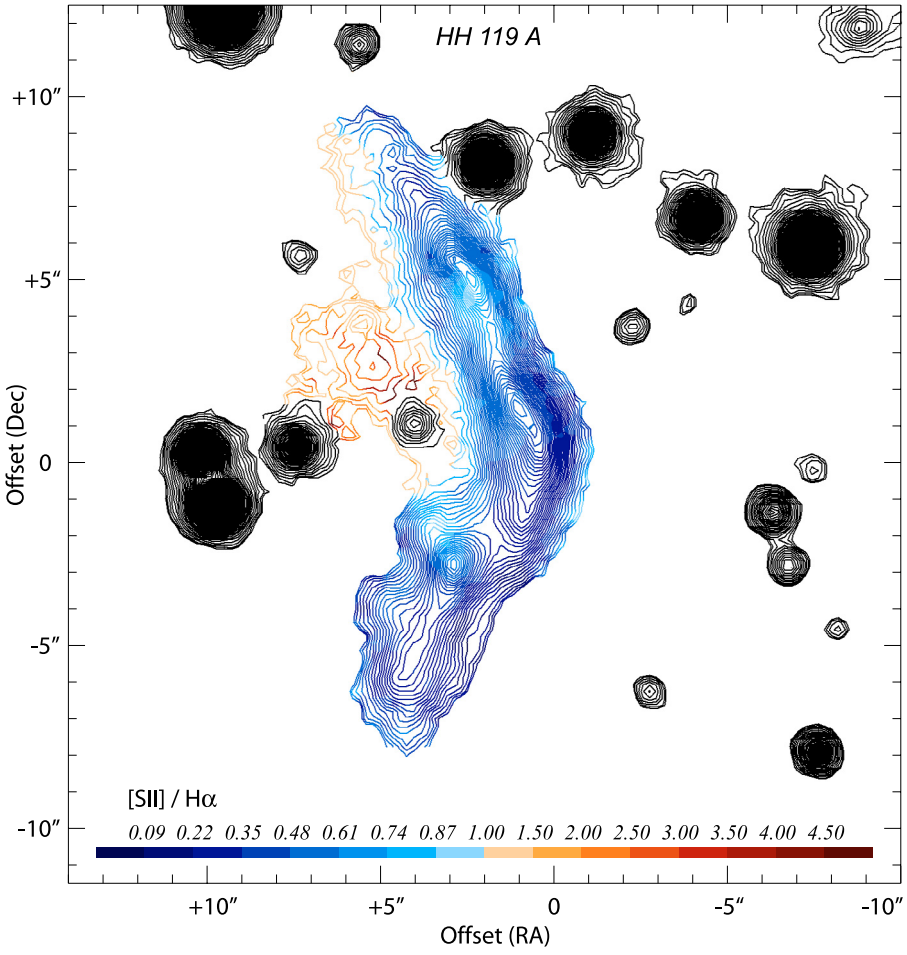

Fig. 9. Detailed overview of HH 119 A simultaneously showing a Hα+[SII] surface brightness map (contours) and the excitation structure by colouring the contours based on the [SII]/Hα ratio. Note that the colour coding is totally independent of the contours, this means that any given contour can have any variation of colours ([SII]/Hα) along its curve. Stars are also included in this plot, these however have black contours. HH 119 A is centred so that its brightest position is roughly located at zero offset. The faintest Hα+[SII] contour shown has a surface brightness of about 8.4 × 10^{-17} erg s^{-1} cm^{-2} arcsec^{-2}.

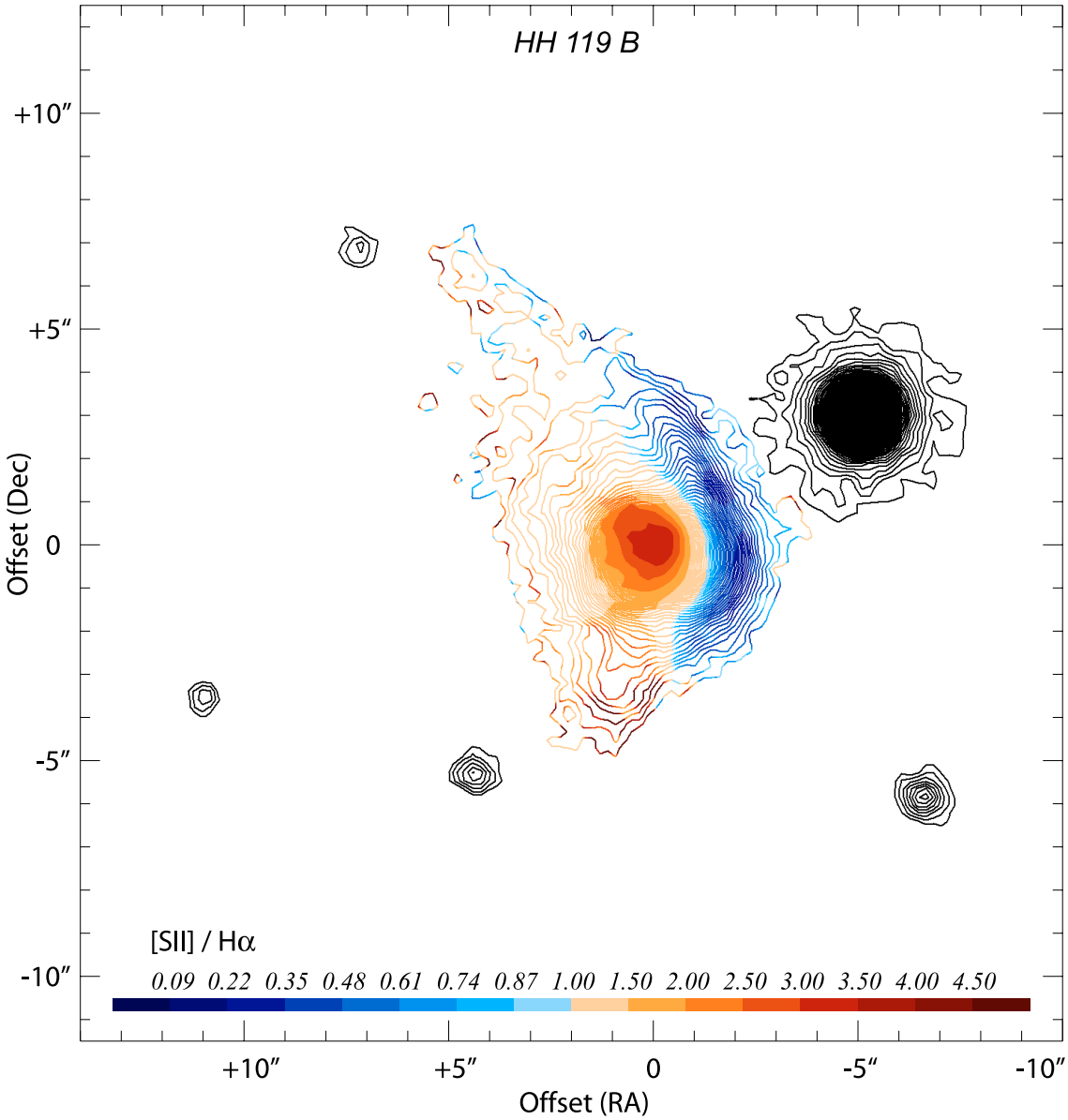

Fig. 10. Detailed overview of HH 119 B, using the same technique as in Fig. 9. HH 119 B is centred so that its brightest position is roughly located at zero offset. The faintest Hα+[SII] contour shown has a surface brightness of about 3.1×10^{-17} erg s^{-1} cm^{-2} arcsec^{-2}.

much higher preshock density n_0 than object A, which might be expected given its location much closer to the centre of the globule where the density is higher.

3.6. Near-UV imaging

In Fig. 11 our U band deep field is presented. HH 119 A is clearly detected, and has a very similar appearance to its Hα counterpart. After background subtraction of the scattered starlight in the globule we also detect HH 119 B and E but these are however much fainter than object A in the near-UV. For object B this is expected because of its much higher extinction ($\Delta A_V \approx 3$). None of the other HH objects are detected, but for HH 119 C and D this could partly be explained by their proximity to a bright star combined with the seeing in the near-UV.

The transmission curve of the U filter is shown in Fig. 6 together with the atmospheric transmission for the mean airmass of the observations, the detector QE and the total system transmission (black solid curve). There are probably only two spectral features that contribute to the U band flux of these HH objects. The [OII] λ3728 line, located close to the maximum system transmission, which has also been shown to be strong in other HH objects (see e.g. Hartigan et al. 1999) and the blue continuum from two-photon emission. The blue continuum spectral distribution has been plotted in Fig. 6 using a blue dashed curve with a scale corresponding to the percentage of its peak value. The total U band flux for the three detected HH objects are given in Table 3.

3.7. Spitzer mid-IR imaging

Figure 15 shows our Spitzer 3.5, 4.5 and 8.0 μm IRAC composite of B335. An hourglass-shaped reflection nebula is clearly seen in the centre (at 4.5 and 8.0 μm), with an outflow cone to each side of the central VLA source (IRAS 19345+0727), marked by a cross in the figure. Most of the HH objects we see in our optical and near-IR deep fields can also be seen in the 4.5 μm channel of Spitzer (green in the colour composition used in Fig. 15).

Table 7. Extinction and shock model results for HH 119 A, B and C.

Iteration step	$(H\alpha/H\beta)_0$	A_V[a] (mag)	$E(B-V)$ (mag)	n_0[b] (cm^{-3})	C[c]	Ionization I[d] (%)	$\langle I\rangle$[e] (%)	Shock velocity V_S[d] ($km\,s^{-1}$)	$\langle V_S\rangle$ ($km\,s^{-1}$)
(1)	(2)	(3)	(4)	(5)	(6)	(7)	(8)	(9)	(10)
					HH 119 A				
Initial guess[f]	3.00	1.65	0.53	625	20	...	2.0	...	30.0
Iteration	3.34	1.31	0.42	25	40	40.0, 23.0, 13.5	25.5 ± 14	74.7, 60.2, 46.4	60.4 ± 15
Result	**3.29**	**1.36**	**0.44**	**23**	**40**	**40.0, 30.0, 13.5**	**27.8 ± 14**	**74.7, 68.7, 45.3**	**62.9 ± 16**
					HH 119 B				
Initial guess[f]	3.00	5.59	1.80	8400	15	...	1.0	...	30.0
Iteration	4.33	4.44	1.43	1530	25	3.1, 2.2, 4.6	3.3 ± 1.3	37.8, 34.6, 39.8	37.4 ± 2.7
Result	**4.33**	**4.44**	**1.43**	**1070**	**28**	**3.7, 3.6, 5.2**	**4.2 ± 1.0**	**37.1, 35.7, 38.0**	**36.9 ± 1.5**
					HH 119 C				
Initial guess[f]	4.33	(4.44)[g]	(1.43)[g]	930	15	...	1.0	...	30.0
Iteration	4.18	(4.44)[g]	(1.43)[g]	100	28	6.1, 4.1, 6.1, 3.3	4.9 ± 1.5	43.6, 37.7, 38.1, 33.5	38.2 ± 4.2
Result	**4.38**	(4.44)[g]	(1.43)[g]	**83**	**23**	**8.6, 7.6, 7.7, 5.5**	**7.3 ± 1.5**	**41.9, 37.2, 33.3, 26.9**	**34.8 ± 6.4**

[a] Using the extinction law of Cardelli et al. 1989, $R_V = 3.1$ and $(H\alpha/H\beta)_{obs}$.
[b] Preshock density, $n_0 = (n_e/\langle I\rangle)/C$.
[c] Shock compression.
[d] Estimates from line ratios [OI] 6300/Hα, [SII] 6717+31/Hα, [NII] 6583/[OI] 6300. For HH 119 C also from [NI] 5200/[NII] 6583.
[e] [SII]-weighted ionization fraction $\langle I\rangle$.
[f] Initial guesses taken from objects with similar excitation, HH 47 jet (HH 119 A) and HH 34 jet (B and C). See Hartigan et al. (1994).
[g] Since Hβ is not detected from HH 119 C, the extinction is *assumed* to be the same as for HH 119 B (see text).

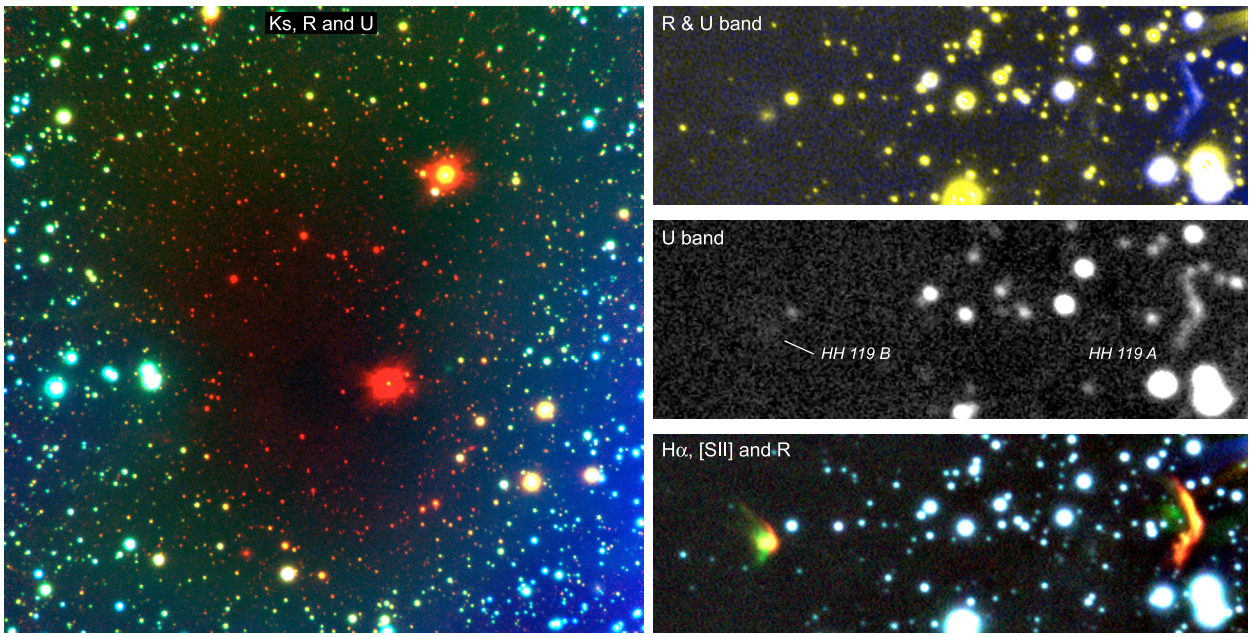

Fig. 11. Near-UV deep field. A composite of K_S (red), R (green) and U (blue) mosaics (*left panel*). The cloud extinction is effectively shown using this filter combination, spanning from the near-UV to the near-IR. After removing the background from scattered starlight in the U mosaic, three of the HH objects are detected (HH 119 A, B and E). In the *right panel* we show several filter combinations using background subtracted mosaics. It is clear that the appearance of object A is very similar in the U and Hα filters. The field of view is $4\farcm25 \times 4\farcm13$ in the left panel and $116'' \times 39''$ in each of the right panels.

Note that, except for the strong artefacts seen close to bright stars (to the SSW) in this filter, all these extended objects are most likely HH objects. These include all HH objects A–H, except HH 119 C, which is too close to a bright star for detection. HH 119 I is located outside the Spitzer image.

It has been shown in several other Spitzer surveys (e.g. Noriega-Crespo et al. 2004; Harvey et al. 2006; and Gålfalk & Olofsson 2007) that the IRAC channel centred at 4.5 μm is very efficient in detecting bona-fide Herbig-Haro objects. The reason for this is partly that the spectral response function is highest in this channel, but there are at least two more contributing factors. Between approximately 4–5 μm there are many vibrational and rotational H_2 emission lines, these have been modeled by Smith & Rosen (2005) for all IRAC bands using three-dimensional hydrodynamic simulations of molecular jets. The strongest integrated H_2 emission is predicted to arise from band 2 because of rotational transitions. For the typical conditions of low-mass outflows, pure-rotational transitions like S(11)–S(4) (4.18–8.02 μm) can actually be much brighter than the standard 2.12 μm H_2 line (Kaufman & Neufeld 1996). Channel 2 is also the most "PAH-free" band of IRAC, greatly enhancing its usefulness as a HH tracer, as opposed to the 5.8

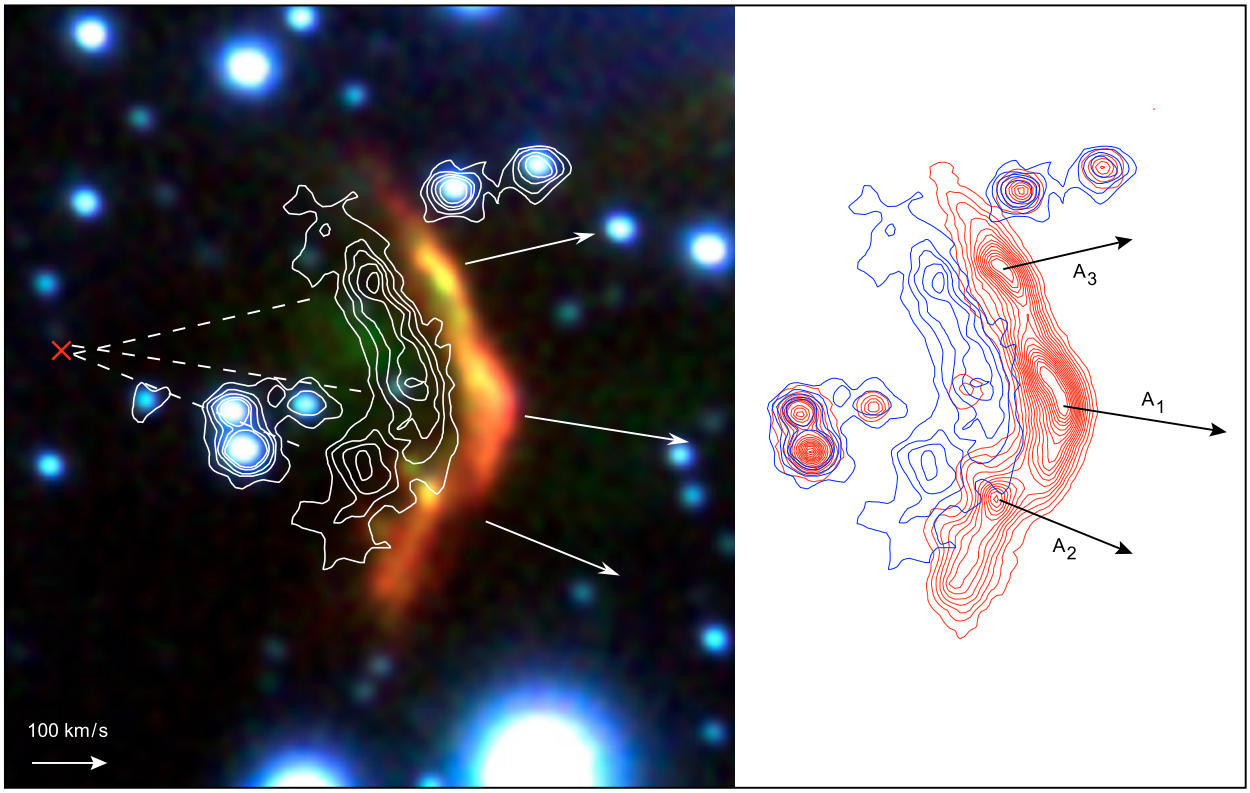

Fig. 12. Optical close-up of the HH119 A shock in Hα (red), S[II] (green) and *R* (blue). The overplotted Hα contours from the first epoch (15 years earlier, Reipurth et al. 1992) clearly illustrates the movement of this shock. Proper motions have been calculated for three Hα peaks in the shock (A_1, A_2 and A_3) as shown by the arrows. The shock is clearly expanding much faster than would be suggested by its position in relation to the outflow source if a linear expansion was assumed. The field size in the left panel is $25\farcs9 \times 27\farcs8$.

and 8.0 μm channels which have very high background contrasts caused by extended Polycyclic Aromatic Hydrocarbon (PAH) emission, hiding the shock-excited H_2 features of the HH flows.

A closer inspection of our IRAC composite actually reveals one more extended object with strong 4.5 μm flux, this object is located to the east of HH 119 E and F, at a declination that is consistent with it being part of the HH flow. It is located just outside the eastern border of our 2.12 μm mosaic but a faint object is hinted at this position in our Hα mosaic, although very close to the border where the S/N is degraded due to the few number of overlapping exposures used in that part of the mosaic. Given its location and brightness in the Spitzer image, together with its Hα detection (although faint), we classify this as an HH object (HH 119 H).

We identify a very red object to the north in Fig. 15 as HH 119 VLA 2 (Avila et al. 2001), also known as Barn 335 3 (Anglada et al. 1992). The nature of this source is unknown. It is located outside the northern border of our 2.12 μm H_2 S(1) mosaic and no Hα emission is seen near this object.

3.8. Individual Herbig-Haro objects

Figure 5 shows all the HH objects in detail with individually adapted contrast. In this section details of each HH object will be discussed, referring to Fig. 5 in the following if the image of a shock is discussed without further reference.

3.8.1. HH119 A and IR 7

The image of HH 119 A has been deconvolved using maximum entropy to bring out more details, made possible by the high S/N ratio achieved for this object. The leading bow shock is dominated by Hα emission (even though there is considerable [SII] emission as well) followed by a region dominated by [SII] emission. There are three condensations (emission peaks) in the bow shock, called A_1 (middle peak), A_2 (south) and A_3 (north).

We have measured the proper motions within the bow shock using the three Hα peaks. The result is shown in Fig. 12 with projected velocities illustrated by arrows. The image is an extreme close-up of the HH 119 A part of our deep field, with overplotted Hα contours adapted from Fig. 2 of Reipurth et al. 1992. Note that even though the northern condensation (A_3) may seem to move in a slightly different direction (not as far north) than the arrow implies in the left panel of Fig. 12, this is just a visual effect caused by both Hα and S[II] being shown as red and green, respectively, in the colour composite. The proper motions were calculated from the locations of the Hα emission knots, as shown in the right panel.

We note that the central peak found in the first epoch image coincides with a star behind the shock that is now revealed 15 years later. The Hα contribution from this star in the first epoch is unknown, but a wider peak has been used to trace the proper motion of the middle part of the shock in order to minimize the risk of confusion with this star.

The bow shock is clearly expanding at a much faster rate than would be expected by its distance from the outflow source

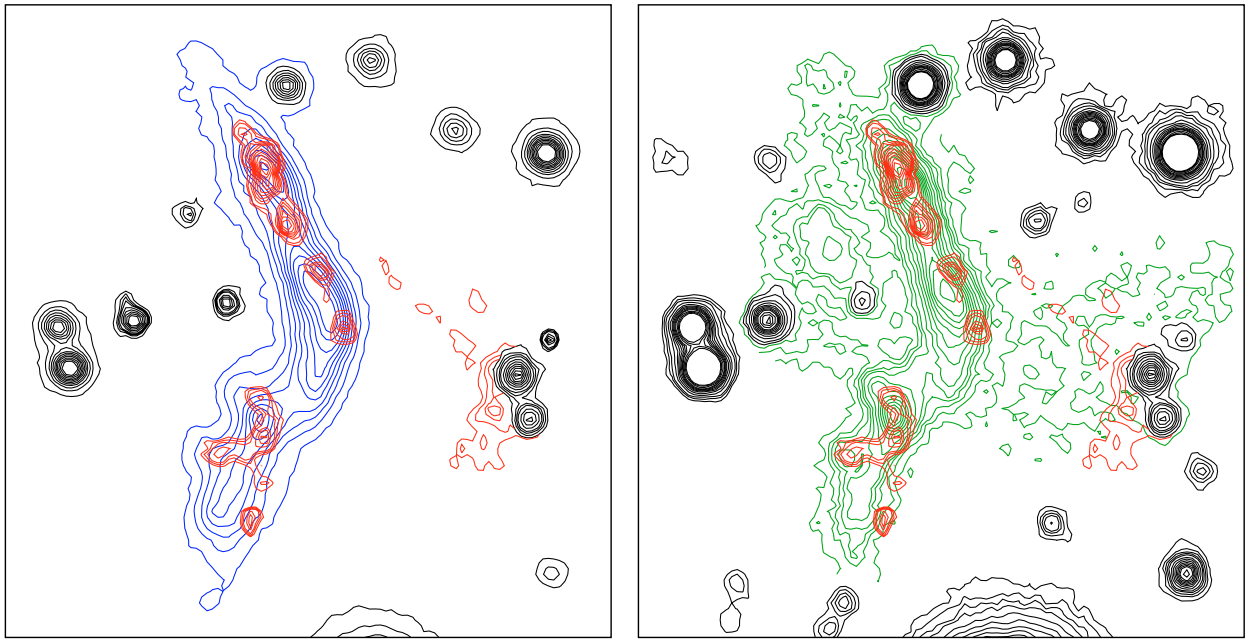

Fig. 13. HH 119 A flux contours in Hα (blue), S[II] (green) and S(1) (red). The contour levels have been chosen to emphasize the different features seen in each transition. It is clear that most S(1) knots in HH 119 A lie well within the optical bow shock. In S[II] there are two more features when compared to Hα, a bright trailing structure and an extended faint feature in front of the bow. This feature can also be seen faintly in S(1) as a bow-shaped object leading the main optical bow shock. Stars have been coloured black. The field size is $21'' \times 21''$ in both panels.

assuming a linear expansion, since tracing the arrows backwards leads to a point much further west than the outflow source (Figs. 3 and 12). The expansion rate has thus increased with time as the shock gradually moves into less dense parts of the globule, approaching free expansion. Object B has a similar appearance to object A, albeit on a smaller scale, suggesting the amount of expansion between these positions in the flow. The situation is reminiscent of the HH34 jet and bow shock (Figs. 9 and 10 of Reipurth et al. 2002a) where the width of the jet and the size of HH objects increase with distance along the jet from the outflow source.

The spectrum of HH 119 A_2 (Fig. 7) shows strong Hα and weak [SII] emission, HH 119 A is thus a high excitation object as opposed to the other HH objects for which we have optical spectra. The first detection of Hβ in object A is also seen in this spectrum.

The picture of HH 119 A as a coherent bow shock (as seen in Hα) is not always true. We detect the S(1) counterpart of object A as broken up into three parts (IR 7a–c, see Fig. 2). In Fig. 13 we plot flux contours in Hα, [SII] and the S(1) line. It is evident that most of the S(1) knots in the northern and southern part (IR 7a and b) lie well within the contours of the optical bow shock. There is also a third, very faint counterpart in S(1) (IR 7c), also bow-shaped, which preceeds the optical bow. Comparing the [SII] and S(1) contours (right panel) we see that, not only is there extended [SII] emission in a cooling zone behind the bow shock, there is also a faint [SII] structure preceeding the bow, at the position of IR 7c.

3.8.2. HH119 B and IR 1

HH 119 B is a nice well-defined bow shock with Hα followed by [SII] emission, and an apex with both strong Hα and [SII] emission. The shock follows in the wake of HH 119 A, which is a possible explanation why the spectrum of this shock shows a lower excitation (see Fig. 7). The spectrum also shows object B to have strong [OI] $\lambda\lambda$ 6300/63 emission lines, which was not the case in the Aug. 1990 observations of Reipurth et al. (1992). The conditions in object B have apparently changed during the 13 years between the two epochs.

The near-IR H_2 S(1) source IR 1 has a similar position and proper motion position angle as object B, although their proper motions differ by more than 70 km s^{-1}. To clarify the situation a colour composite using both the optical and near-IR shock observations has been made (Fig. 14, right panel) by warping the S(1) image to match the pixel size and distortion of the optical images (Hα and S[II]).

These shocks are likely physically connected, with the S(1) bright shock IR 1 located in the southern part of optically bright shock B. While their difference in projected velocities suggest that their alignment could be merely coincidental, the most likely situation is that they are in fact counterparts of the same object, since IR 1 is located far out in the wing of bow shock B where the (projected) shock speed is much slower than at the apex. This could explain the S(1) brightness if H_2 is not disassociated in the bow wing. The geometry and expected excitation structure (Fig. 14) thus suggest that IR 1 is the near-IR counterpart of HH 119 B.

3.8.3. HH119 C, D and IR 5

In the image of object C in Fig. 5, a bright star has been removed at the position marked by a plus sign in all three filters (Hα, [SII] and *R*) using the PSF of a similarly bright star, lowering the contrast considerably and making it possible to display HH 119 C in much more detail. A star, not seen prior to the PSF removal, is also revealed very close to the north of the removed bright star (at the edge of the black circle).

This is the first detection of object D in the optical, it had only been seen faintly in the near IR prior to this paper (IR 5). Our near-IR observations show this to be a bow shock at 2.12 μm H_2 as well. Object D has a complicated excitation structure, as

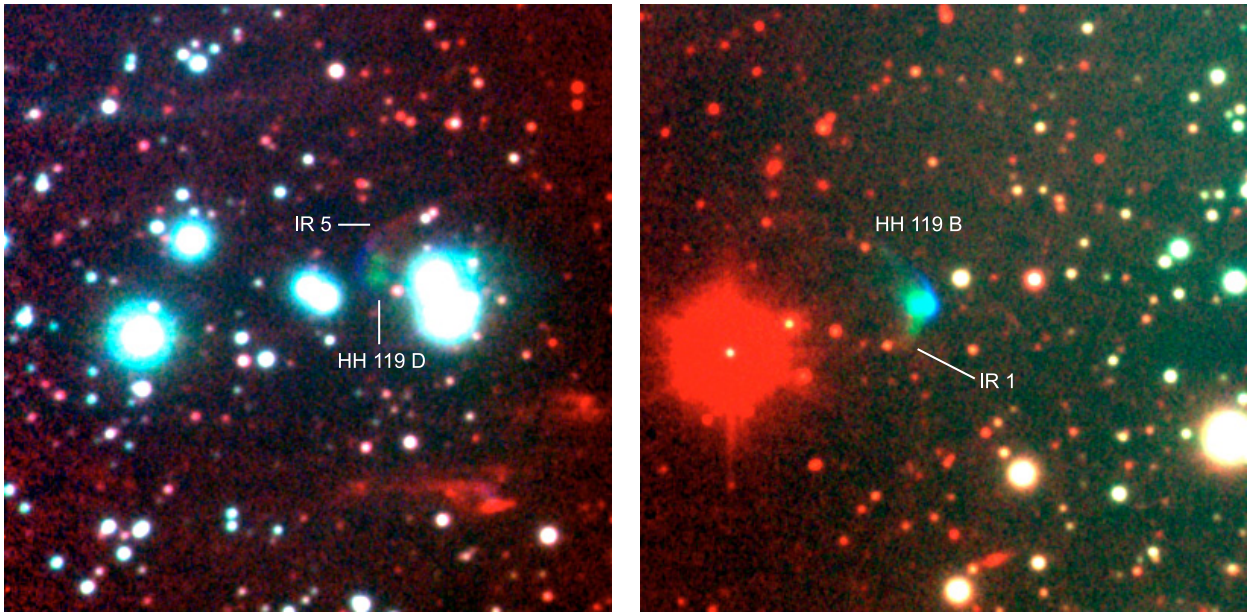

Fig. 14. Optical and Near-IR composites of HH 119 D / IR 5 (*left*) and B / IR 1 (*right*) using a Hα (blue), [SII] (green) and 2.12 μm H_2 (red) colour coding. In both shocks the optical shock emission is clearly strongest close to the apex of the bow shock, Hα at the front and [SII] in the cooling zone behind it. The near-IR shock emission is displaced to the north and south in HH 119 D and B, respectively. In the case of HH 119 D, the near-IR shock is also bow-shaped, but located further to the north. The near-IR counterpart of HH 119 B, IR 1, does not have the appearance of a bow, it does however coincide with the far southern wing of the optical bow shock, as might be expected since the projected shock velocity (perpendicular to the bow surface) is much lower far out in the wing than at the apex. Both fields have a size of $75'' \times 75''$.

suggested by the optical/IR composite image (Fig. 14). A leading bow-shock dominated by Hα is clearly seen, followed by two well-defined "sulphur bullets" in the complicated cooling zone and a near-IR H_2 bow shock, displaced to the north relative to the optical bow shock. The situation appears to be similar to that of objects B and IR 1, with a S(1) strong part of the bow shock far out in the (north) wing where the projected shock speed is much lower than at the apex of the bow shock.

3.8.4. HH119 E, F, H and IR 6

Both HH 119 E and F are previously undetected Herbig-Haro objects. As can be seen in the image, they both have separated nebulous features between filters in the direction expected if they originate from the central outflow source. HH 119 F is seen as a Hα bow shock, followed by a similar S[II] feature. It resembles a smaller version of HH 119 B moving approximately ESE, as suggested by its structure and supported by its proper motion. HH 119 E is probably moving almost exactly to the east, as it is perfectly lined up with HH 119 A–D and the outflow source. As seen in the image for object E, and suggested by the optical spectra of other HH objects in this flow (B and C), object E must have very strong [OI] $\lambda\lambda$ 6300/63 emission (as the leading shock is strongest in the *R* band) followed by a Hα shock.

There is another, although very faint, Hα feature to the east of these objects in the HH flow but mid-way between them in declination. This object, HH 119 H, is however clearly seen at 4.5 μm using Spitzer (IR 6 in Fig. 15). Details about this object are given in Table 2.

3.8.5. HH119 G, IR 2, 3 and 4

In the blue-shifted lobe we find IR objects 2–4 moving as a group roughly to the ESE. Except for the brightest S(1) peak, IR 4a (G), these objects are only seen in the near-IR deep field. They all have slower projected velocities than the A–D optical bipolar flow, and especially features 3 and 4 have much slower space velocities.

As suggested by the Spitzer image (Fig. 15) these shocks could be the result of turbulent interaction of molecular material from the surrounding cloud and the outflow, near the cavity walls. This interaction could be what is slowing down the outflow and creating these shocks. The reason why they are only seen in the near-IR could be a combination of extinction and the amount of H_2 relative to atoms and ions (such as H, S+ and O). In a slow magnetically supported (C-type) shock, molecules are not as dissociated as in fast (J-type) shocks. IR 2 is moving much faster than objects 3 and 4, in a direction more to the east, within the cone that has already been cleared out by the outflow.

3.9. HH119 I and the IR 8 system

In our 2007 images of western B335 we see a very likely counterflow (Fig. 2) to the ESE flow, consisting of a system of at least 15 H_2 knots. Careful image re-reduction of our optical deep field close to the mosaic edge, where the signal is lower due to few overlaps and the flatielding is very sensitive to vignetting, revealed an optical (Hα and [SII]) counterpart, HH 119 I (Fig. 4), to one of these H_2 knots. This WNW counterflow (although no proper motions are known yet) is, similar to the ESE flow, much brighter in S(1) than at Hα or S[II] when compared to HH 119 A–F in the E–W flow. The detection of this system and the similar properties to the ESE flow opens up the possibility that the outflow source may in fact be a binary source, with two slightly different oriented outflow axes giving rise to these two flows.

Fig. 15. Spitzer IRAC composite of B335 using a 3.5 μm (blue), 4.5 μm (green) and 8.0 μm (red) colour coding. The red plus sign marks the central VLA source position. There is a clear correlation between the bipolar cone-shaped structure seen at these wavelengths (3.5–8.0 μm) and the VLA source position. Many of the HH objects and S(1) knots seen in our optical and near-IR mosaics are also detected at 4.5 μm (IRAC channel 2) which is clearly the most efficient channel for tracing the flows.

4. Summary and conclusions

In an effort to investigate the Herbig-Haro flows in the nearby dark globule B335, a well-studied protostellar collapse candidate with three previously known HH objects, we have taken optical spectra and observed an optical tri-colour deep field (Hα 6.7 h, [SII] 6.2 h and R 39 min) and a near-IR bi-colour deep field (2.12 μm H_2 S(1) 6.5 h and K_S 48 min), as well as an additional near-IR field of western B335, using the 2.56 m Nordic Optical Telescope and a near-UV deep field (U band 7.4 h) with the 3.58 m New Technology Telescope. In addition we present new SPITZER / IRAC (3.5, 4.5 and 8.0 μm) and MIPS (24 μm) observations. The following results were obtained:

1. We discover five new HH objects (HH 119 D–H) in the blue-shifted (eastern) lobe and one new HH object (HH 119 I) in

the red-shifted (western) lobe of the outflow. Two of these HH objects (D and G) have previously observed near-IR counterparts (Hodapp 1998). In our S(1) mosaic we detect these as large extended shocks (object D being a large bow shock). In western B335 we also detect a system of at least 15 previously unknown H_2 knots.

2. By combining our observations with earlier epochs in the optical and near-IR we calculate proper motions of the previously known HH objects (and the new HH 119 F) and 2.12 μm H_2 S(1) knots using a time span of 15 and 9 years, respectively.
3. The combined optical and near-IR proper motion maps, together with the deep images, show that the opening angle of the bipolar flow is already very wide and reveals two sub-groups within the flow, a high velocity bipolar flow (space velocities 200–280 km s^{-1}) in the E–W direction (HH 119 A–F) that is bright in optical shock lines, and a much slower flow (15–75 km s^{-1}) in the ESE direction within the blue lobe (HH 119 G and IR 2–4) that is bright in the S(1) line. We also propose a counterflow in a roughly WNW direction (red lobe), also bright in S(1) and faint in Hα and [SII].
4. All proper motion vectors originate from central B335. We suggest two possibilities, either the E–W and ESE−WNW shock groups belong to the same outflow but are flowing in different parts of a cone-shaped cavity cleared out by the outflow, or the outflow source is binary in nature resulting in two outflow axes with slightly different orientations.
5. Two of the new HH objects, HH 119 E/F, are equidistant to HH 119 A from the outflow source, while HH 119 C/D are roughly equidistant to HH 119 B. The bipolar E–W flow is thus roughly symmetrical, with two outburst episodes suggested, 255 and 645 years ago, respectively, from proper motions. The conclusion that the central source has undergone several eruptive events has previously been suggested by Reipurth et al. (1992) who also used proper motions to estimate these two outburst ages (they estimated 350 and 850 years).
6. For HH 119 A, the proper motions of three Hα condensations show that the shock is rapidly expanding, at a much faster rate than would be expected from a linear expansion given its distance from the outflow source.
7. The [SII] / Hα structure of the shocks indicate that the ESE group rams into a denser ambient medium, with the situation being the opposite for the E-W flow.
8. Our optical spectra show HH 119 A to be of higher excitation than B and C (which are both low excitation objects). We detect Hβ for the first time in both A and B, making it possible to estimate the extinction towards these HH objects. In stark contrast to a previous spectrum of HH 119 B, we detect strong [OI] $\lambda\lambda$ 6300/63 emission lines. It is clear that object B must have changed a lot during the last decade or so.
9. We calculate the optical extinction towards HH 119 A and B to be $A_V \approx 1.4$ and 4.4, respectively.
10. Using planar shock models we have estimated the shock properties of HH 119 A–C. The resulting shock velocities are much lower (a factor 5−10) than the space velocities found through proper motions. This is however very common for Herbig-Haro objects, and expected when gas with high space velocity is caught up by slightly faster gas, making the relative (shock) velocity lower than the space velocities. This is also the case in bow shocks, where the shock velocity is lower in the wings than at the apex of the bow since the projected velocity perpendicular to the shock is highest at the apex and lowest far out in the wings. We find shock velocities of ∼60 km s^{-1} (A) and ∼35 km s^{-1} (B and C). This agrees well with object A being of higher excitation, and B following in the wake of this object. The [SII]-weighted ionization fraction is also found to be much higher in object A.
11. We detect HH 119 A, B and E in the U band after background subtraction of scattered starlight throughout the globule. This emission is proposed to be a combination of two spectral features, the [OII] λ3728 line and the blue continuum.
12. Most of the HH objects and S(1) knots are detected in the SPITZER / IRAC observations (channel 2, 4.5 μm). An hour-glass shaped feature is seen in the IRAC images, centred on the VLA outflow source, with a morphology that agrees with a cone-shaped E–W flow. Even at 24 μm it is unclear whether most of the light is direct or reflected, a single peak can be seen but it is offset by about 2.″8 to the SE from the VLA position.

Acknowledgements. The Swedish participation in this research is funded by the Swedish National Space Board. This publication made use of the NASA/IPAC Infrared Science Archive, which is operated by the Jet Propulsion Laboratory, California Institute of Technology, under contract with the National Aeronautics and Space Administration, and data products from the Two Micron All Sky Survey, which is a joint project of the University of Massachusetts and the Infrared Processing and Analysis Center/California Institute of Technology, funded by the National Aeronautics and Space Administration and the National Science Foundation. We would like to thank Klaus-Werner Hodapp, Institute for Astronomy, University of Hawaii for providing the 2.12 μm H_2 mosaic we used as the first epoch in our proper motion calculations. We would also like to thank Bo Reipurth, Institute for Astronomy, University of Hawaii for providing us with the first epoch Hα images we used in our optical proper motion calculations. Also, we want to thank Sven Olofsson, Stockholm Observatory, for providing us with the U band image.

References

André, P., Ward-Thompson, D., & Barsony, M. 1993, ApJ, 406, 122
Anglada, G., Rodríguez, L. F., Cantó, J., et al. 1992, ApJ, 395, 494
Avila, R., Rodríguez, L. F., & Curiel, S. 2001, Rev. Mex. Astron. Astrofis., 37, 201
Cardelli, J. A., Clayton, G. C., & Mathis, J. S. 1989, ApJ, 345, 245
Chandler, C. J., Gear, W. K., Sandell, G., et al. 1990, MNRAS, 243, 330
Frerking, M. A., & Langer, W. D. 1982, ApJ, 256, 523
Frerking, M. A., Langer, W. D., & Wilson, R. W. 1987, ApJ, 313, 320
Gålfalk, M. 2005, NOT Annual report 2004, 18
Gålfalk, M., & Olofsson, G. 2007, A&A, 466, 579
Hartigan, P., Morse, J. A., & Raymond, J. 1994, ApJ, 436, 125
Hartigan, P., Morse, J. A., Tumlinson, J., et al. 1999, ApJ, 512, 901
Harvey, D. W. A., Wilner, D. J., Lada, C. J., et al. 2001, ApJ, 563, 903
Harvey, D. W. A., Wilner, D. J., & Myers, P. C. 2003, ApJ, 583, 809
Harvey, P. M., Chapman, N., Lai, S.-P., et al. 2006, ApJ, 644, 307
Hodapp, K. W. 1998, ApJ, 500, L183
Kaufman, M. J., & Neufeld, D. A. 1996, ApJ, 456, 611
Keenan, F. P., Hibbert, A., Ojha, P. C., et al. 1993, Phys. Scr., 48, 129
Keene, J., Davidson, J. A., Harper, D. A., et al. 1983, ApJ, 274, L43
Morse, J. A., Heathcote, S., Cecil, G., et al. 1993, ApJ, 410, 764
Morse, J. A., Hartigan, P., Heathcote, S., et al. 1994, ApJ, 425, 738
Noriega-Crespo, A., Morris, P., Marleau, F. R., et al. 2004, ApJS, 154, 352
Ramsbottom, C. A., Bell, K. L., & Stafford, R. P. 1996, Atomic Data and Nuclear Data Tables, 63, 57
Reipurth, B. 1983, A&A, 117, 183
Reipurth, B., Heathcote, S., & Vrba, F. 1992, A&A, 256, 225
Reipurth, B., Heathcote, S., Morse, J., et al. 2002a, AJ, 123, 362
Reipurth, B., Rodríguez, L. F., Anglada, G., & Bally, J. 2002b, AJ, 124, 1045
Smith, M. D., & Rosen, A. 2005, MNRAS, 357, 1370
Tomita, Y., Saito, T., & Ohtani, H. 1979, PASJ, 31, 407
Vrba, F. J., Luginbuhl, C. B., Strom, S. E., et al. 1986, AJ, 92, 633